

REPORT DOCUMENTATION PAGE			Form Approved OMB No. 0704-0188	
Public reporting burden for this collection of information is estimated to average 1 hour per response, including the time for reviewing instructions, searching existing data sources, gathering and maintaining the data needed, and completing and reviewing the collection of information. Send comments regarding this burden estimate or any other aspect of this collection of information, including suggestions for reducing this burden to Washington Headquarters Services, Directorate for Information Operations and Reports, 1215 Jefferson Davis Highway, Suite 1204, Arlington, VA 22202-4302, and to the Office of Management and Budget, Paperwork Reduction Project (0704-0188), Washington, DC 20503.				
1. AGENCY USE ONLY (Leave blank)		2. REPORT DATE 4/22/99		3. REPORT TYPE AND DATES COVERED 5/95-9/98
4. TITLE AND SUBTITLE High Resolution Computerized Ionospheric Tomography Systems			5. FUNDING NUMBERS 1.- N00014-95-1-0850 2.- N00014-97-1-0419	
6. AUTHOR(S) Helen Na				
7. PERFORMING ORGANIZATION NAMES(S) AND ADDRESS(ES) University of Iowa 201 Gilmore Hall Iowa City, IA 52242 N00014-95-1-0850 UCLA Regents of University of California, Los Angeles 405 Hilgard Ave. Los Angeles, CA 90095 (N00014-97-1-0419)			8. PERFORMING ORGANIZATION REPORT NUMBER HN-ONRYI	
9. SPONSORING / MONITORING AGENCY NAMES(S) AND ADDRESS(ES) Office of Naval Research Ballston Tower One 800 North Quincy St. Arlington, VA 22217-5660			10. SPONSORING / MONITORING AGENCY REPORT NUMBER	
11. SUPPLEMENTARY NOTES Attached papers				
a. DISTRIBUTION / AVAILABILITY STATEMENT Public Distribution			12. DISTRIBUTION CODE	
13. ABSTRACT (Maximum 200 words) Research has focused on the development, characterization and implementation of algorithms for time varying ionospheric imaging. Several techniques were used including neural network based approaches for imaging localized time varying events, an iterative volumetric approach for three-dimensional imaging that enables localized incorporation of a priori information, and a technique that utilizes both TEC data as well as information from the WSBI system. Considerable effort was made to analyze the strengths and weaknesses of the various approaches and their inherent limitations. Tests were made using both real and simulated data.				
19990505 102				
14. SUBJECT TERMS Computerized Ionospheric Tomography			15. NUMBER OF PAGES 87	
			16. PRICE CODE -	
17. SECURITY CLASSIFICATION OF REPORT Unclassified	18. SECURITY CLASSIFICATION OF THIS PAGE Unclassified	19. SECURITY CLASSIFICATION OF ABSTRACT Unclassified	20. LIMITATION OF ABSTRACT UL	

This research progressed simultaneously in several directions. Details of each area of research are discussed below.

First, we developed a novel neural network based approach to imaging ionospheric motion. The algorithm employs neural networks as estimators of a time varying electron density distribution; however the networks are not used to estimate the electron densities directly but rather the change in electron densities at each time step.

At each time step, the method consists of four main parts. First, a ray tracing procedure is used to calculate ray path information for the current time step; this information is used to determine the expected measurement values based on the last time step. Second, the expected measurement values are subtracted from the actual measurement values. This information, along with the ray path geometry, is then preprocessed so that it can be used by the neural network. Third, the neural network is trained using the pre-processed data. Fourth, the network is used to produce an electron density estimate for the current time step.

Preliminary experimental results indicate that ionospheric electron density estimation using this method is both computationally feasible in real time and capable of producing reasonable reconstructions given the proper choice of neural network. In particular, a two layer neural network trained using the Levenberg-Marquardt method was found to be capable of locating a localized time-varying Gaussian depletion type ionospheric disturbance based only on very sparse data.

Second, we have worked on the development of a new fully 3D reconstruction algorithm for CIT, capable of combining some of the available measurement sources in order to compensate for the unavoidable physical limitations of the acquisition system.

The main features of the algorithm are:

a) Fully 3D reconstruction with arbitrary voxel size. b) Real-time system geometry computation in spherical coordinates. c) Direct (non-iterative) reconstruction based on a least-squares inversion method. d) Physical constraints (e.g. non-negativity of the electron density) and RADAR measurements (e.g. WSBI data) introduced as boundary conditions for the least-squares algorithm. e) No a priori information on the electron density distribution required. f) Ready for acquisition system extension to occultation measurements. When satellite occultation TEC measurements will become available an interface is ready to include them in the reconstruction algorithm system matrix. g) Choice of parameters is minimized. Raw estimates of the measurement errors are the only parameters necessary to run the whole algorithm. At this time most of the software features are operative. The package includes a fast 3D ray-tracing algorithm capable of computing a system matrix with arbitrary voxel sizes in real time and storing it in a compressed sparse form.

The bounded least squares problem engine has been tested and optimized for the given problem. A technique to improve the sparseness of the intermediate results generated in the inversion process is under construction. This represents at the moment the factor that limits the size of the system matrix, which can be used without incurring in unacceptable memory requirements.

The inclusion of non-TEC measurement data, e.g. WSBI data, is under development in this stage. On the other side the algorithm gave very promising results simply adding some simple physical constraints in the reconstruction algorithm.

Third, we developed the multi-input volumetric inversion algorithm (MIVIA). After algorithm development, the goals of the research were to test its reliability and performance for various types of CIT system geometry and various ranges of regulatory parameters.

Sensitivity Analysis of MIVIA involved a three phase sequence of tests for determining parametric sensitivity, convergence sensitivity and sensitivity to a priori information. The volumetric inversion algorithm was designed to select a priori information based on guidance from TEC measurements obtained during the CIT satellite overpass. Volumetric information is supplied to the reconstruction in the projection and image domains of each iteration. Investigation of the relative strengths of projection and image domain corrections yielded optimal values of 1 for projection domain shaping and 0.01 times the order of maximum electron density for image domain shaping. Consequences of excessive image domain shaping in instances of low sky coverage were also demonstrated including the case of over correction that results in the inversion of image features. Convergence was achieved faster in the vertical direction than along the horizontal because of the dual support of ray path profiles and image neighborhood shapes in the former. Horizontal convergence supported only by image domain shaping and is typically achieved between 40-50 iterations as opposed to 10-15 iterations for vertical convergence. With respect to a priori input, it was observed that reconstructions preserved features of the parent image when aided by relatively smooth and featureless a priori images. Such supportive information is crucial to the formation of the vertical profile and is used based on the need for such information during the localized volumetric shaping processes.

A considerable amount of work was performed on estimating reconstruction artifacts that arise because of non-ideal system geometry and incomplete recording of an overpass from individual stations. Various pathological instances of imperfect system geometry were developed including isolated non-coplanar receivers, satellite orbits longitudinally displaced from receiver chains and of narrow ray path beams from certain stations. Among the important observations on artifact formation was that displacement of an individual station from an otherwise coplanar receiver chain results in an elevation of features in the reconstruction in over the latitudes in which the displaced stations ray fan plays a dominant role. Artifacts such as false enhancements and troughs were found to form because of abrupt termination of ray fans particularly in the center of the image plane. It was also observed that if geographic logistics prohibit the placement of

a receiver chain directly below the satellite path, the quality of reconstructions is significantly improved by positioning at least one additional receiver in the orbital plane. Such a co-planar receiver provides invaluable support to the set of largely slant TEC ray paths in the projection set.

A scheme for the quantitative evaluation of the features of an ionospheric image were also developed with the aim of providing an objective and automatic analysis of image content. Histogram redistribution techniques were developed to separate a typical ionospheric electron distribution into enhancements and horizontally stratified bands. In addition extremely localized searches were devised to identify travelling ionospheric disturbances which are usually invisible to the human eye because of the dynamic range of the entire image. Geometric and electron density based properties of image regions corresponding to features such as peaks and horizontal bands were derived and used for the comparison of images. It is anticipated that this quantitative scheme will permit further advanced evaluation of CIT inversion techniques by comparing reconstructions by various algorithms using the same TEC data set or for comparing CIT reconstructions to gold standards such as images obtained using the incoherent scatter radar technology.

Finally, we worked on developing and implementing CVT (CREDO-VSIRT Technique), studies on the incorporation of WSBI data into VSIRT, and reconstructions for simulated and real data.

The studies on the incorporation of WSBI data into VSIRT entailed understanding the weaknesses of both CREDO and VSIRT, and finding ways to use the strengths of each for the benefit of better reconstructions. Some of the techniques include the initial guess method, the control point method and the method of doing the WSBI inversion within VSIRT.

In the area of reconstructions, the most important result was the simulated test of detecting an E-layer using VSIRT. This test proved that VSIRT was able to pick up an E-layer, but it was only able to do it in a very controlled environment, i.e. ideal station alignment and an E-layer that was quite high in altitude.

Technical details are provided in the enclosed papers.

Estimating dynamic ionospheric changes without a priori models

Robert A. Granat,¹ Helen Na

University of California, Los Angeles, Los Angeles, California

Short title: ESTIMATING IONOSPHERIC CHANGES

Abstract. We present a novel artificial neural network based computerized ionospheric tomography (CIT) technique, capable of imaging through time in three dimensional space. Total electron content (TEC) data collected from a satellite passing over the region of interest is used to train a neural network. The trained network creates estimates of the difference in ionospheric electron density between time steps based on the TEC data. Application of the difference estimate at each time step to the previous electron density image results in a time varying ionospheric electron density estimate. Experimental results on synthetic data are presented that demonstrate that the algorithm is capable of detecting short-term localized disturbances in the ionosphere.

1. Introduction

Although accurate information about ionospheric electron densities is crucial for correcting radio signal aberrations, the ionosphere is far from static, varying even within the time scale of a single satellite pass over the region of interest. Natural effects such as diurnal variation along the day/night boundary, solar radio emissions, solar flares, volcanic eruptions, earthquakes, and geomagnetic storms can all affect the dynamics of the ionosphere within minutes. Rapid perturbation of the ionosphere can also result from man made effects such as chemical and nuclear explosions and high-powered radio waves.

Current measurement techniques are unable to provide the necessary information about ionospheric electron densities. As a result, it is necessary to use computational methods to transform measurement data into images of ionospheric electron densities. The use of such computational techniques is referred to as computerized ionospheric tomography (CIT).

The majority of current CIT algorithms are only capable of reconstructing static images of the ionosphere. However, when static CIT algorithms are applied to a dynamic ionosphere, the clash between the assumption of time invariance made by these algorithms and the time dependency of the actual electron density results in estimation errors. These errors include clearly visible artifacts, such as streaking, negative ionospheric density values, and geometric distortion (i.e., features displaced from their actual position) [Sutton and Na, 1998].

In order to avoid such errors, it is necessary to use time varying CIT (TVCIT) algorithms capable of estimating ionospheric electron densities as they evolve in time. Methods have been presented that attempt to estimate time varying ionospheric images [Sutton and Na, 1998; Howe et al., 1998]. However, these methods are critically dependent on a priori models of ionospheric structure. As a result, ionospheric motion and structure that does not fit the a priori models may be ignored or misinterpreted.

Unfortunately, it is exactly this kind of unpredictable or unknown behavior that it is most desirable to detect.

This problem stems ultimately from the underdetermined nature of the system. The above methods attempt to address the lack of data by making use of empirically derived basis functions. However, in doing so they compromise their ability to detect novel or unusual ionospheric structure and activity. In this paper we present an alternative artificial neural network based technique capable of imaging through time in three dimensional space. The neural network based method attempts to preserve the ability to detect interesting ionospheric phenomenon, while avoiding the problem of data scarcity. Because the data is so sparse, it is extremely difficult to accurately compute the electron density at any point in the image. Instead, we seek to generate estimates of the ion density based on what little information is available. In principle, artificial neural networks are well suited to this kind of estimation because they have the ability to generalize results based on a small subset of the data.

2. Computerized Ionospheric Tomography

A minimum data collection system used for CIT consists of a radio beacon satellite orbiting over the region of interest and a series of ground station receivers aligned (roughly) along the satellite path. The system collects measurements of total electron content (TEC) by means of the Doppler radar technique. Two signals are sent out at frequencies high enough to linearly penetrate the ionosphere; the phase difference at each ground station receiver provides a measure of the TEC along the ray path from the satellite to that station. This TEC measurement is approximately the line integral of electron densities along the ray path.

Figure 1

Figure 1

The first CIT reconstruction technique was introduced by Austen et al., 1986. Since that time, a number of CIT techniques have been devised and experiments in various

locations around the world have been conducted.

3. Neural Network Approach to TVCIT

The artificial neural network is not used to estimate the electron density directly but rather the change in the electron densities at each time step. If the time step used is sufficiently small, then the difference in ion density between time steps should be minor. Thus, the problem can be broken down into a series of relatively small estimation problems.

At each point in time, the algorithm proceeds through four main steps. First, a ray tracing procedure is used to calculate ray path information for the current time step; this information is used to determine the expected TEC values based on the last time step. Second, expected TEC values are subtracted from the actual measured TEC values for the current time step; this information, along with the ray path geometry, is preprocessed so that it can be used by the neural network. Third, the neural network is trained using the preprocessed data. Fourth, the network is used to create the electron density estimate for the current time step.

The algorithm assumes that a good initial estimate is available at the start of the procedure. Although this is a significant assumption, there are a few practical methods by which this initial estimate could be obtained; these will be discussed later.

Aside from an initial estimate, the algorithm also requires system geometry information and TEC measurement data. The geometry is determined by the satellite position and ground stations positions. The TEC measurement data is collected by the ground stations at select time intervals.

4. Algorithm Details

Given the system geometry and TEC data, the first step in the reconstruction process is the calculation of the ray path information. In general in tomography

problems one seeks to calculate a system matrix (either explicitly or implicitly) which contains information about the ray paths through the region being imaged. In the ionospheric tomography case, at each instant in time there is a spread of ray paths from the satellite to each of the ground stations. The data used is collected from within a given time window. Once that time window has been selected, it is necessary to calculate a system matrix describing the ray paths from each of the satellite positions to the ground stations. Calculating the system matrix in general involves some form of ray tracing. In this case, the ray tracing procedure is somewhat involved due to the nature of the spherical coordinate system used by the simulation.

The ray path information is then used to calculate expected TEC values given the electron density distribution of the previous time step. These expected values are then subtracted from the measured TEC values to produce TEC difference values.

The next step of the algorithm consists of preprocessing of the ray path and measurement data. Preprocessing of the data is necessary because the artificial neural network is expected to approximate the change in ion density as a function of spatial position. As such, it requires as its input pixel coordinates and outputs the corresponding electron density change value. This requires that the data (i.e., the total electron content measurement differences and system matrix) be used to generate pixel values on which to train the artificial neural network. This is done by calculating the the minimum norm solution to the underdetermined equation

$$\mathbf{Ax} = \mathbf{b},$$

where \mathbf{A} is the sparse system matrix, \mathbf{b} is a vector containing the TEC difference measurements, and \mathbf{x} is a vectorized representation of the image. The resulting solution vector \mathbf{x} contains the training output values, each of which corresponds to a non-zero element of the system matrix. The coordinates of the non-zero elements are the training input values. Note that these are only the pixel values along the ray paths; the procedure

is not capable of calculating of calculating pixel values elsewhere in the image.

Once the experimental data has been preprocessed into the correct form, it can be used to train the artificial neural network. The network has three inputs, one for each of the coordinate values, and a single output unit for the electron density change. The output unit has a linear response so that it is capable of representing any value. The number and nature of the hidden units varies by the approach used.

The network is then trained using the Levenberg-Marquardt method. An alternative to the gradient descent based backpropagation method, the Levenberg- Marquardt algorithm is theoretically faster and potentially more accurate, although it requires more storage space for the computation.

The Levenberg-Marquardt algorithm can be used as an approximation to the Newton method. The weight update rule is

$$\Delta \mathbf{W} = (\mathbf{J}^T \mathbf{J} + \mu \mathbf{I})^{-1} \mathbf{J}^T \mathbf{e},$$

where \mathbf{W} is a matrix of weights w_{ij} connecting two layers, \mathbf{J} is the Jacobian matrix of derivatives of each error to each weight, \mathbf{e} is an error vector, and μ controls the learning rate.

If μ is very large, the update approximates gradient descent; if it is small the update approximates the pure Newton method. The Newton method approximation is faster, but tends to be less accurate when near the minima. To deal with this problem, the parameter μ is adjusted in an adaptive fashion. If the error is decreasing, μ is made bigger; if the error is increasing, μ is made smaller.

When training is complete, a complete estimated ion density change image can then be created. The coordinates of each pixel are given as input to the net and the output is assigned as the pixel value, thus forming a complete image. The electron density change image can then be added to the previous electron density image to produce the current electron density image.

5. Experimental Results

Experimental results for the algorithm were generated using simulated volume data along with ground station positions and satellite paths from an ongoing campaign in the Caribbean region.

The simulation included an ionospheric disturbance, a Gaussian depletion of the electron density. Initially, there was no activity. Then a region of increased electron density was introduced, followed soon after by a neighboring region of decreased electron density.

Figures X.X and X.X show a longitudinal slice of the electron density image produced by the simulation before the disturbance.

Figure 2 figure 3

ionospheric density estimation problem appears to yield good localization of an ionospheric disturbance, as long as some of the ray paths pass close enough to the disturbance for it to affect the measurement data.

Figure X.X shows the output of the Levenberg-Marquardt trained network with ten neurons given four ray paths, one of which passes close enough to the Gaussian depletion to detect it at that time step. Figure 4.15 should be compared to figure X.X, which displays the ground truth electron density change for the same time and longitudinal slice. Although the electron density change is more distributed than in the ground truth, the peak of the density change is located in the correct spot.

Figure 4 Figure 5

Figures X.X-X show the output of that same network at the 1st, 7th, and 16th longitudinal slices, along with their associated ground truths. Note that the electron density is located correctly in longitude as well as in latitude and altitude.

Figure 6 Figure 7 Figure 8 Figure 9 Figure 10 Figure 11

The method suffers from the fact that the number of hidden units must be chosen carefully. If too few hidden units are used, the resolution is insufficient; if too many

Figure 2

figure 3

Figure 4

Figure 5

Figure 6

Figure 7

Figure 8

Figure 9

Figure 10

Figure 11

hidden units are used the network overfits the data and estimate becomes distorted and irregular.

As well, good convergence via the Levenberg-Marquardt method is sensitive to the random initialization of the neural network weights. Therefore, for the ionospheric reconstruction system to produce reliable results, it is necessary to repeatedly train the network at each time step. The result at a given time step with the least error is then used. Although this still does not guarantee a good approximation (it might be that a poor choice of random starting weights is made each each try), it would greatly reduce the probability of a poor approximation. The number of tries can be adjusted according to the required confidence in the results.

However, such an approach increases the amount of computation. Fortunately, training the network using the Levenberg-Marquardt method takes considerably less time than generating the complete ion density estimate from the trained network. On the order of ten training attempts can be made without adversely affecting the speed of the algorithm to a significant degree.

6. Conclusions and Future Work

We have presented a novel neural network based CIT method capable of imaging ionospheric electron densities across time and three dimensional space. In experiments using simulated electron density data and realistic CIT system geometries, the algorithm has proven capable of estimating the location and magnitude of regional transient disturbances in ionospheric electron density. The method has the advantage of not relying on a priori models of the ionosphere, thereby giving it the capability to detect unusual or unexpected ionospheric phenomenon. Furthermore, the computation can be performed in real time, making it amenable to field application. The method is extensible as well in that it can be easily modified to use additional data sources, such as ionosonde readings or total electron content measurements garnered from GPS satellites.

Still, some improvements suggest themselves with regard to this TVCIT method. The sensitivity of the method to the random initialization can be mitigated by developing a system which attempts to pick the best result from an array of estimates generated by different initializations. Or alternatively, if the time resolution is sufficiently fine, then the electron density change can be considered continuous in time, and information about the motion in previous times could be used to initialize the network weights for the current time step.

As well, possible overfitting of the neural network to the limited data could be reduced. This could be done by sampling the data according to ray path coverage density, or by taking advantage of the extendability of the method and adding additional data sources.

Effective initialization of the algorithm remains the most pressing problem. In the experiments discussed previously, a good initial estimate was assumed. However, a poor estimate can ruin the results of the algorithm. Incoherent scattering radar measurements could provide a good initial estimate; however in the absence of such generally available measurements it is necessary to develop a more general initialization method.

Three such methods suggest themselves. The first would be to start with a set of a priori images, chosen appropriately for the geographical placement of the region of interest. The method could then be initialized with the a priori image that most closely matches the measurement data from the first time step.

The second approach would be to collect measurement data for some amount of time as the satellite begins its pass over the region of interest. A standard non-time varying CIT technique could then be used to create a reconstruction using the data collected from the beginning of the pass; the resulting image could then be used to initialize the algorithm.

The third method would only be applicable in a scenario where repeated experiments are conducted. During the first satellite pass, only a static reconstruction would be

performed. This static reconstruction would then be used to initialize the time varying algorithm for the next satellite pass.

Acknowledgments.

This work was supported by the Office of Naval Research under grants N00014-95-0850 and N00014-97-0419 and by the National Science Foundation under grant ATM9696259.

Thanks also goes to Dr. Gary Bust of the University of Texas, Austin, who provided the synthetic ionospheric data.

References

- Austen, J. R., S. J. Hranke, and K. C. Yeh, Ionospheric imaging using computerized tomography, *Radio Science Journal*, 23, 299-307, 1988.
- Fremouw, E. J., J. A. Secan, and B. M. Howe, Application of stochastic inverse theory to ionospheric tomography, *Radio Science*, 27, 721-732, 1992.
- Howe, B. M., K. Runciman, and J. A. Secan, Tomography of the ionosphere: Four-dimensional simulations, *Radio Science*, 1, 109-128, 1998.
- Sutton, E., and H. Na, Time Varying Reconstruction of the Ionosphere: Part 2. Data Source Analysis, *Int'l J. of Imaging Systems and Technology*, 9, 484-490, 1998.
- Sutton, E., and H. Na, Time varying reconstruction of the ionosphere: Part 1. The algorithm, *Int'l J. of Imaging Systems and Technology*, 9, 491-499, 1998.

R. Granat and H. Na, Department of Electrical Engineering, University of California, Los Angeles, Los Angeles, CA (email: granat@icsl.ucla.edu; hna@icsl.ucla.edu)

Received _____

¹Also at the Jet Propulsion Laboratory, Pasadena, California.

To appear in *Radio Science*, 1999

Figure 1. A simple CIT system.

Figure 2. A 2-dimensional view of the 10th longitudinal slice of the simulated electron density.

Figure 3. A 3-dimensional view of the 10th longitudinal slice of the simulated electron density.

Figure 4. 10th longitudinal slice of the electron density change estimate.

Figure 5. 10th longitudinal slice of the simulated electron density change.

Figure 6. First longitudinal slice of the electron density change estimate.

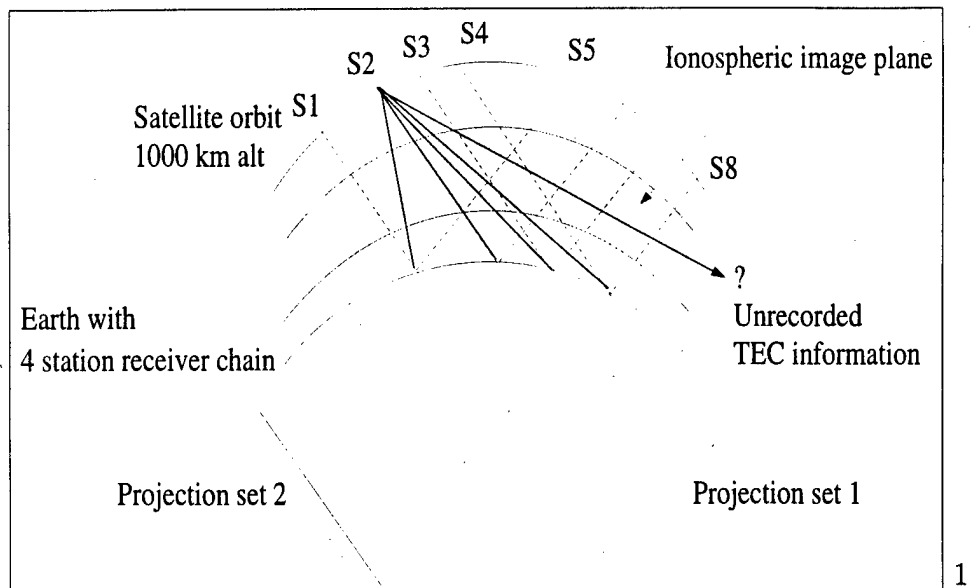
Figure 7. First longitudinal slice of the simulated electron density change.

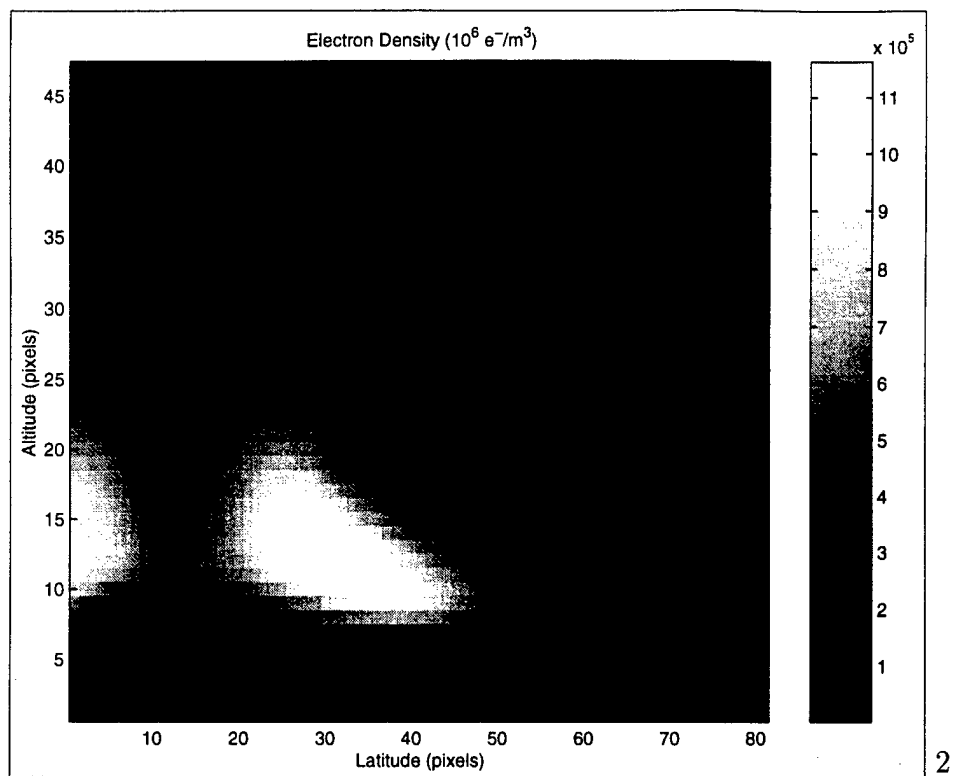
Figure 8. 7th longitudinal slice of the electron density change estimate.

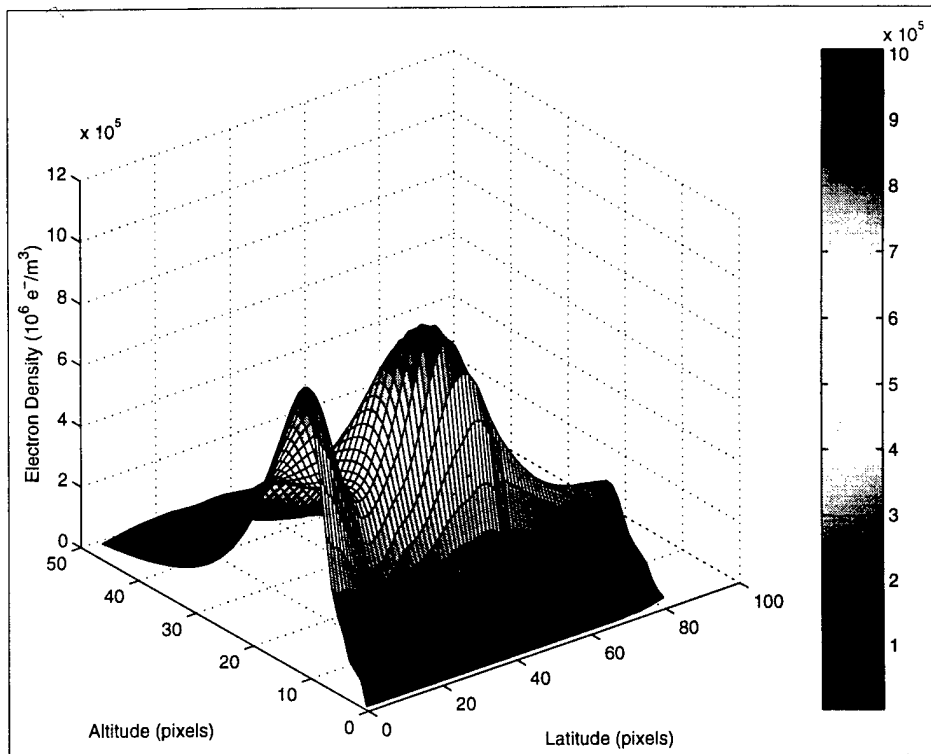
Figure 9. 7th longitudinal slice of the simulated electron density change.

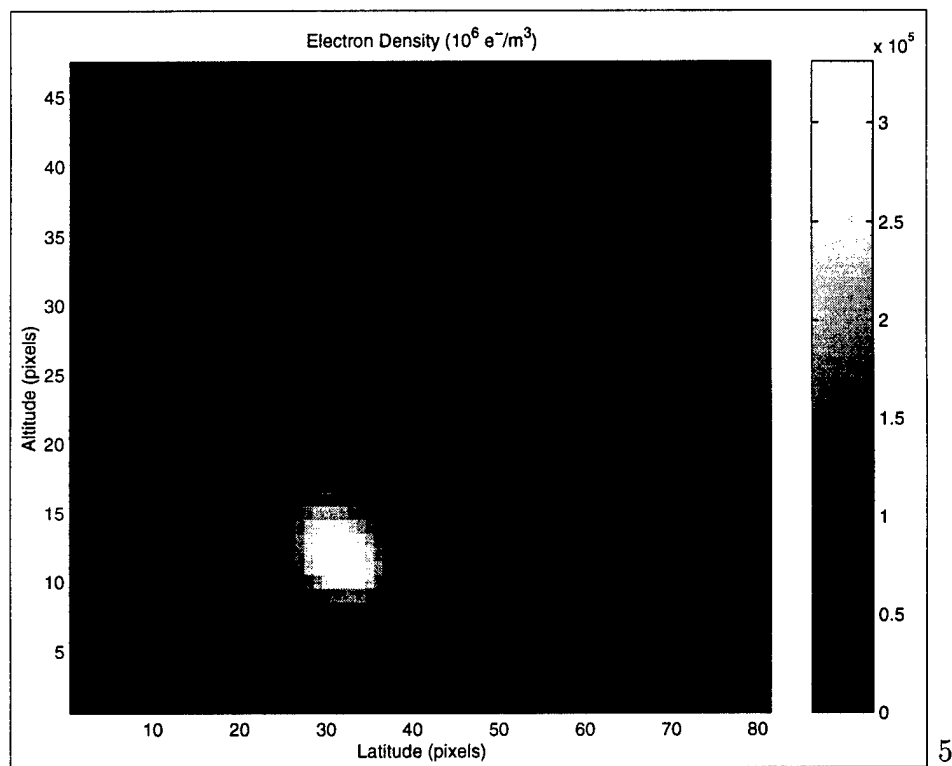
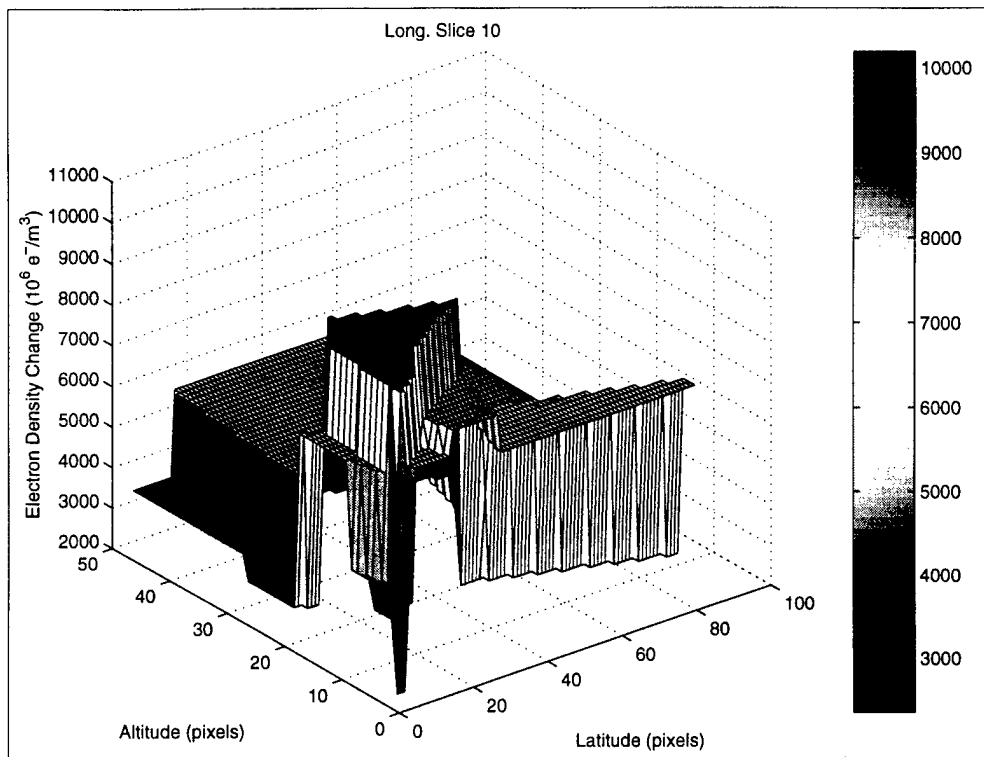
Figure 10. 16th longitudinal slice of the electron density change estimate.

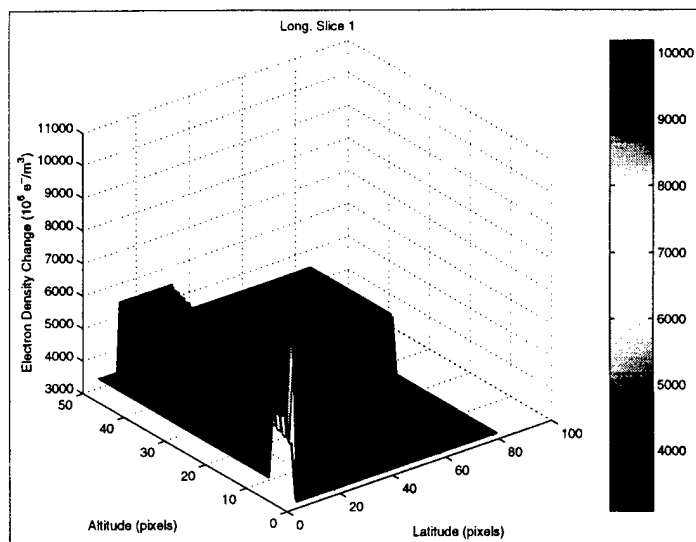
Figure 11. 16th longitudinal slice of the simulated electron density change.

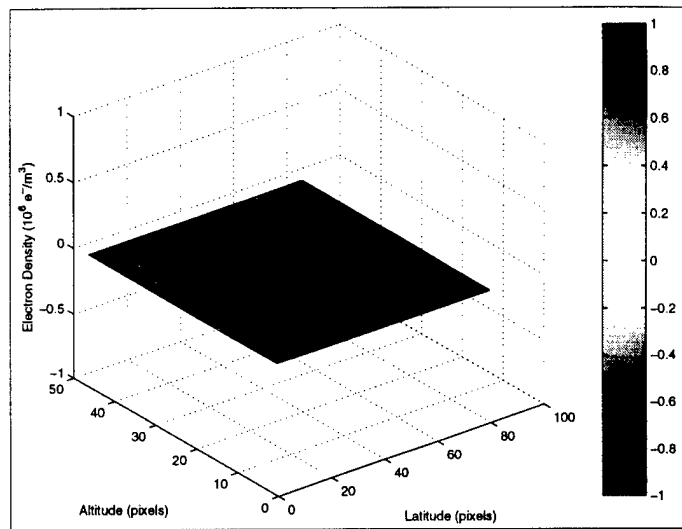


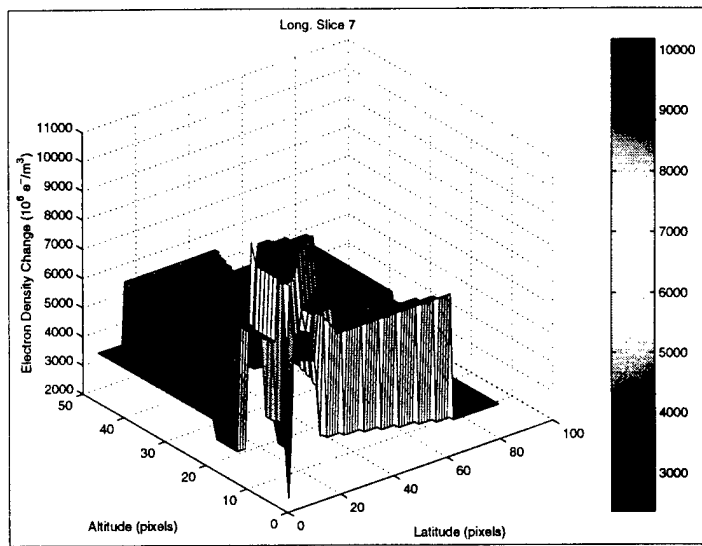


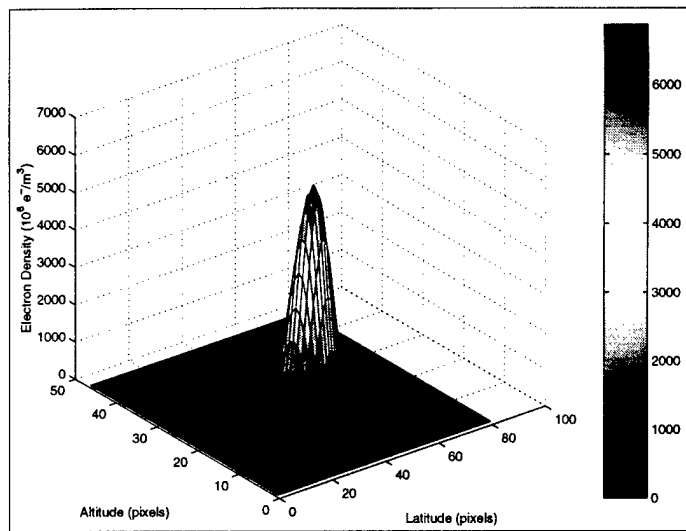


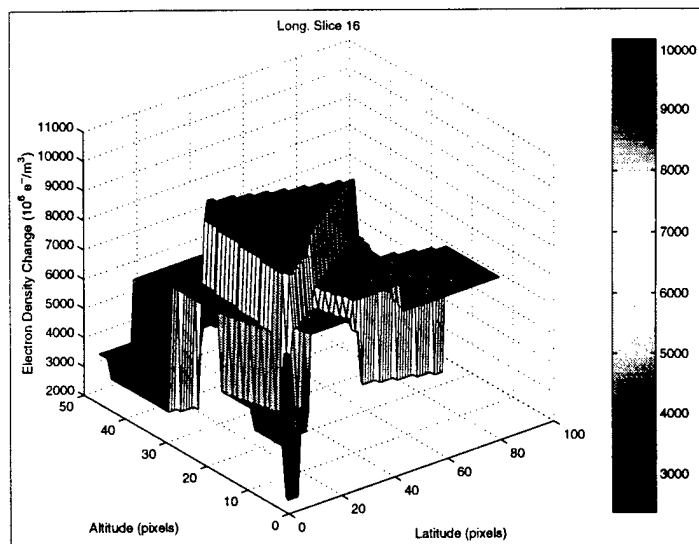


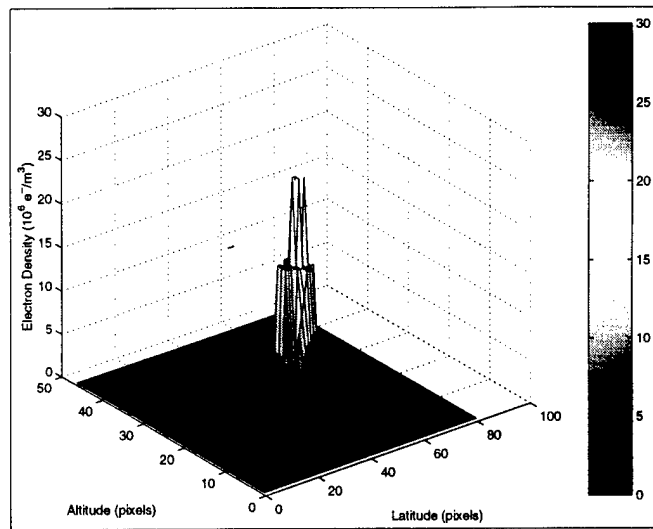












Resolution and coverage analysis for ionospheric tomography

Chaitali Biswas and Helen Na

Department of Electrical Engineering

University of California, Los Angeles

Abstract

This paper presents results of investigations on the relationship between optimal image resolution and associated sky-coverage for ionospheric tomography. Several measures of the variation of image information content as a function of resolution have been presented for understanding the nature of tradeoffs between information content and computational resources. A new quantitative description of imaging geometry enables sky-coverage analysis for this limited information tomographic system. The paper also presents examples of commonly encountered non-ideal system geometries, diagnosis of associated image artifacts, and improvements achieved by minor logistic modifications to the imaging system.

1. Introduction

Computerized ionospheric tomography (CIT) [Austen *et al.*, 1988] provides an excellent opportunity for observing the relationship between the information content registered by a limited angle, limited data tomographic imaging system and the subsequent information distribution achieved in the tomographic inversion process. The availability of records from numerous experimental campaigns conducted over the past decade and the emergence of applications such as over-the-horizon radar provide additional incentive for the study of information flow in restricted tomographic systems. Knowledge of information availability and distribution in limited information systems is expected to contribute significantly to diverse pursuits ranging from optimization of computational resources to the diagnosis of misleading features of artifacts in the reconstructions. This paper is concerned with two specific sets of CIT related analyses governed by tomographic information content, namely, image resolution analysis and sky-coverage based image artifact analysis.

Ionospheric tomography involves registration of the phase difference between two radio signals from a low-orbit satellite by one or more chain of ground based receivers. The phase difference being representative of the total electron content (TEC) along the corresponding signal ray-path through the atmosphere, the recorded data can be processed using tomographic principles to reconstruct a two or three-dimensional image of the ionospheric region lying between the satellite and the ground stations. Due to geometric restrictions such as the curvature of the earth and continuity of the atmospheric shell around it and logistic restrictions such as the limited availability and irregular, non-coplanar positioning of receivers, CIT is effectively a limited angle, limited sample tomographic system. In addition to the above mentioned static restrictions, variations in receiver operation often result in dynamic limitations such as loss of

absolute phase related information [Leitinger, 1994] and the incomplete recording of satellite overpasses from individual stations. Therefore the comprehensive study of information registration and distribution would involve quantitative definitions of ray-path distribution or sky-coverage in the ionospheric region of interest. The optimal resolution of reconstructed images in limited angle and limited sample imaging systems is governed by sky-coverage. In addition, the distribution of sky coverage itself can be related to the formation of image artifacts because it is effectively a measure of limited visibility of the object distribution.

The remainder of this paper is organized into four sections. A more detailed description of sky-coverage and the image coordinate system are presented in section two. Sections three and four discuss the important results and observations made in the process of image resolution and image artifact analysis based on sky-coverage. The concluding section consists of discussions on the significance of information content evaluation and artifact diagnosis for limited angle tomographic systems and on directions for future research in this area.

2. The Coordinate System, Coverage and Imaging Geometry

Traditionally CIT systems have used satellites with polar orbits and therefore ground based receiver chains have usually been oriented in a roughly north-south direction. An exhaustive study of experimental imaging geometries used over the past decade shows major digressions from the assumptions of chain linearity and coplanarity of ground stations and the orbital plane [Biswas, 1999]. Apart from irregular latitudinal spacing of receivers and longitudinal displacement of individual stations from the orbit plane, there exists a wide variation of ground chain distributions and alignments, the usage of multiple chains and the inclusion of multiple satellite orbits in the imaging process. Further more, it is necessary to make provisions

for the usage of non-polar satellites in future systems. The practice of converting non-coplanar or slant ray-paths to vertical coplanar ray paths together with adjustments of TEC values involves geometric and electron density related assumptions and extrapolations [Mitchell *et al.*, 1997]. Recent multiple chain CIT campaigns have used numerical interpolations between a set of verticalized two-dimensional image planes to obtain a three-dimensional reconstruction. However, as demonstrated by a volumetric inversion technique for CIT, it is most convenient to use the true geocentric three-dimensional geometry for CIT imaging since it avoids data preprocessing and permits direct use of slant TEC values. The three coordinates of the geocentric coordinate system are latitude (X-axis), altitude (Y-axis) and longitude (Z-axis). Whereas the resolution can be conveniently varied to desired resolutions with uniformity for the first two coordinates, the latitudinal dependence of longitudinal spacing makes it marginally more computationally intensive to ensure uniform spacing in the Z direction. Fortunately, fairly low resolution of between 3 – 7 planes is sufficient for most CIT imaging systems.

For each satellite overpass, there exists a unique sky-coverage map. Coverage is defined as an image, occupying the same geographic region as the tomographic image, whose voxel value is a count of the number of ray-paths passing through it. Thus the coverage map shows the contribution of information in the most primary sense from various portions of the ionosphere to the TEC data set. Figure 1 shows a diagrammatic comparison between the imaging systems and coverage maps of typical medical and ionospheric systems. The limitations of angular visibility, number and regularity of samples are clearly evident in the second imaging system. The rectangular image of Figure 1d shows curved ray-paths because of the curved to flat earth transformation.

Figure 1

The system devised for the quantitative description of CIT imaging geometry is represented in Figure 2. The suite of coverage parameters, enlisted and explained in Table 1, can be classified into satellite orbit and ground station parameters. These parameters permit characterization and comparison of CIT imaging systems. They have been used in designing several simulated geometries for coverage analysis in section four.

Figure 2

Table 1

3. Resolution Analysis for Ionospheric Tomography

The optimal degree of three-dimensionality for volumetric reconstruction depends on the tradeoff between the feature resolution and information density, that is, coverage. TEC records from four CIT campaigns were analyzed for coverage estimates while varying voxel resolution along various image coordinates for a fixed geographic volume. All four campaigns were conducted in the equatorial and mid-latitudes, hence, there was significant gain in earth-surface resolution with small increments in the number of longitudinal planes. Figure 3 shows the system geometries of the four campaigns which represent the geometric diversity encountered in CIT.

Figure 3

As the resolution was varied along the three geocentric coordinates with geographic resolutions shown in Table 2, there was an initial decrease in coverage with increase in resolution followed by convergence as demonstrated in Figure 4. The point of coverage stabilization was regarded as the optimal resolution along the corresponding coordinate axis for the given CIT geometry.

Table 2

Figure 4

The results of resolution analysis have been presented in Table 3 with Figure 5 highlighting some key observations. Comparing coverage of various image resolutions along the latitudinal and altitudinal directions for the simple, single chain imaging systems of the Mid-American CIT Experiment of 1993 (MACE-93) and the Australian campaign of 1995, it is observed that optimal resolution along the latitudinal direction is governed largely by the

Table 3

Figure 5

displacement of the satellite orbit from the ground station and in the altitudinal direction by the density and linearity of the receiver chain. MACE-93 presented a fairly dense and linear receiver chain but one that was longitudinally displaced from the satellite orbit whereas the reverse was the case with the Australian system. Consequently, there is gainful return for expending computational resources towards improving the resolution along the X axis for the former and along the Y axis for the latter. Data from Table 3 indicates that given typical TEC ray-path density of a CIT system, optimal voxel sizes lie between 111 and 150 km along the X axis on the earth surface and around 20 km along the Y axis or altitudinal direction.

Using a latitudinal resolution of approximately 120 km and altitudinal resolution of 20 km, Figure 6 shows the variation of percentage coverage along each of the longitudinal or Z planes for the four imaging systems. The single most important observation is that even for conventional single chain, single orbit geometries, such as MACE-93 and Australia-95, there is significant coverage in non-central longitudinal planes. This justifies the use of multiple longitudinal planes and hence true three-dimensional coordinates for CIT inversion particularly for multiple chain geometries such as for the ionospheric correction test methods II system of 1996 (ICMT2-96) and of multi-chain, multi-orbit geometries such as used in the Caribbean campaign of 1997. Another noteworthy aspect of Z-plane information is that coverage is highest under orbital planes and the change in sub-orbital coverage is affected to a greater extent by orbit-chain displacement as evidenced by smaller changes in coverage for the Australian campaign than for MACE-93 for Z numbers of 3 and 11.

Figure 6

Although the definition of coverage used in this study did not account for the angular visibility of image voxels and only the percentage coverage was used for resolution analysis, it is an estimate of the absolute maximum information content of the measured TEC data. This study

revealed the significance of system characteristics such as chain linearity and orbital displacement in determining available information content for processing and therefore, in serving as a measure of optimal image resolution.

4. Coverage Analysis for Ionospheric Tomography

A study of several recent CIT campaigns [Biswas, 1999] show that the most common limitations of CIT systems are limited availability and irregular spacing of receivers, longitudinal displacement of individual receivers or the entire station chain from the orbital plane and the incomplete recording of the overpass from individual stations resulting in abrupt edges in the coverage map. In a typical CIT system intended to cover 40-50° of latitude, approximately 1200 project samples are recorded by 4-7 receivers within $\pm 45^\circ$ of the vertical axis of the image. This results in a dense overlap of ray-paths, hence high coverage, in the center of the image which gradually declines to null at either lateral margin of the image providing a U-shaped cone of visibility as shown in Figure 1. In CIT, the typical receiver spacing of 100-300 km on the earth surface is significant when compared with source-receiver separation of only 1000-1200 km. According to the fundamentals of tomography [Kak and Slaney, 1988], such severe undersampling can result in significant reduction in high frequency energy of the projection set and by extension, of the reconstructed image. Images of ionospheric electron content are, by nature, smooth distributions of plasma and of low spatial frequency content. Hence, visual separation of genuine image features from artifacts due to non-ideal sampling for CIT poses an additional challenge. Sky-coverage maps provide useful information about the relative visibility of various regions of the ionosphere to the imaging system during a satellite overpass and can be directly related to the formation of image artifacts.

The principle aim of experiments on sky-coverage for ionospheric tomography was the diagnosis of common image artifacts resulting from non-ideal aspects of the imaging geometry. As discussed in the first two sections, the study was based on devising various pathological situations which further restrict the information content of this inherently limited angle, limited data imaging system of CIT.

Simple geometric images approximating prominent ionospheric formations such as peaks embedded in horizontally stratified layers with or without horizontal gradients were developed for easy diagnosis and appraisal of reconstruction artifacts resulting from the above mentioned limitations. The multi-source volumetric inversion algorithm (MIVIA) [Biswas and Na, 1998a, b] used for the reconstruction process used the test image itself to draw a priori information based on the data obtained in the simulated CIT overpass for various imaging geometries. Volumetric reconstruction uses shape information from electron distributions of the a priori images to guide CIT reconstruction.

Figures 7a through 7e represent the simulated CIT imaging systems and coverage maps associated with the data sets used in reconstructions of Figures 8b through 8f. Despite the close match of a priori and simulated TEC data, the non-ideal geometries of all the systems except that of Figure 7a, result in misleading features or artifacts in the reconstructions. Figure 8a shows the original test image and Figure 8b, the reconstruction obtained with a near-ideal five-station geometry.

The reconstructed image of Figure 8c corresponds to the three-station geometry of Figure 7b where the second station is displaced from the satellite orbit. The coverage from the two sub-orbital stations is incomplete and there is a region above which the only coverage is from the second station. The corresponding region of the reconstruction shows an elevation in the altitude

Figure 7

Figure 8

of horizontal band. This altitudinal shift can be explained by two geometric the two contributing factors as shown in Figure 9. The first of these factors is the increase in the conditional number or the ratio of the largest to the smallest eigenvalue of the sub-system matrix corresponding to ray-paths from the displaced ground stations. As shown in Figure 9a, the farther a receiver is from the satellite orbit, the narrower the angle subtended by a given segment of the orbit on the ground and the smaller the range of angles over which projection sets are available at that site in the tomographic sense. A smaller number of angles given the same number of TEC ray paths accounts for increase in the overall under-determinedness of the inversion problem and translates into lack of tomographic information from the under-represented region of the atmosphere. The second reason for the altitude shift can be attributed to the discretization of the ray-path in the altitudinal direction. Using typical resolutions of 20 km per voxel in the Y direction, the smaller the angle of elevation of the nearest point on the orbit from a ground station, the greater number of longitudinal planes traversed and the greater the cumulative approximations in the estimation of the discretized altitude of features as shown in Figure 9b. In the absence of corrective influences from the sub-orbital stations, the combination of these two factors is responsible for the upward shift of the band in the reconstruction of Figure 8c.

Figure 9

Figures 7c and 8d demonstrate the role played by abruptness of sky coverage, due to the incomplete recording of overpasses, in the development of false distribution features. The northern half of the coverage map is affected by the narrow angular span of coverages from the displaced stations 3 and 4. Relative to the smooth and horizontally homogeneous reconstruction of the southern band in Figure 8d, the northern arm appears to develop variegated regions resembling enhancements and depletions [Davies, 1990] at or around the sites of abrupt coverage. The limitations of sky-coverage is compounded by the non-coplanarity of the stations

in this region which adds to lack of information in the relevant projection sets, and therefore, in the regional density distributions of the reconstructed image.

Figures 8e and 8f correspond to reconstructions of data sets collected using the geometries shown in Figures 7d and 7e. The first imaging system consists of a divergent satellite orbit and receiver chain with the southernmost station as the only sub-orbital receiver. In the second system, the geographic disparity between the satellite orbit and the chain is even more pronounced than in the first except that the second station is now coplanar with the satellite orbit. Preliminary logic suggests that the effect of the greater longitudinal disparity in the second instance would account for poorer coverage and hence, less accuracy in the reconstructions. A comparison of the southern arms of Figures 8e and 8f, however, prove otherwise. This is explained by the fact that central location of the coplanar station in the second instance enables the corresponding ray-path fan to support a greater area both in the latitudinal and altitudinal directions whereas the support of the coplanar station in the first instance is greatly weakened by its location at the edge of the chain. These two geometries are frequently encountered in designing CIT systems where the satellite orbit is largely over vast bodies of water or the orbital plane otherwise inaccessible for receiver deployment. Under such circumstances where a single coplanar receiver may be deployed, better results are obtained by positioning it towards the center of the chain and enabling wider sky-coverage support from the chain.

5. Conclusions

The preliminary experimentation with coverage and image resolution for ionospheric tomography has provided valuable insights into the quality and quantity of information disseminated in the course of image reconstruction. The definition of coverage used in these investigations was a simple and practical estimate of regional availability information in the

visible portion of the atmosphere. It is anticipated that further refinements and usage of this tool will include other tomographically relevant attributes such as angular distribution of ray-paths passing through a voxel. Resolution analysis has demonstrated a simple yet elegant procedure of determining optimal computational resource allocation to meet the changing requirements of this limited angle, limited data imaging system. The development of some commonly encountered coverage related artifacts, which are otherwise difficult to identify given the nature of the fundamental image features, have been traced to specific non-ideal situations created in the sky-coverage of the imaging system. It is anticipated that the quantitative basis for parametric estimation of sky-coverage introduced in this paper will encourage further investigation and understanding of the dissemination of information during the data acquisition and reconstruction process.

The procedures of coverage and resolution analysis presented here are in no way specifically tailored to suit the requirements of CIT. They represent an extremely generalized approach to the understanding of information acquisition and distribution in geometrically restricted tomographic imaging systems, and hence, are applicable to any imaging system with similar limitations.

Acknowledgements

This work was supported by the Office of Naval Research under grants N00014-95-0850 and N00014-97-0419 and by the National Science Foundation under grant ATM9696259.

References

- Austen, J. R., S. J. Franke, and C. H. Liu, Ionospheric imaging using computerized tomography, *Radio Sci.*, 23(3), 299-307, 1988.
- Biswas, C., *Volumetric Reconstruction for Ionospheric Tomography*, (Ph.D. Thesis), University of California, Los Angeles, 1999.
- Biswas, C., and H. Na, Three-dimensional computerized ionospheric tomography using volumetric constraints, *Radio Sci.*, 33(6), 1793-1805, 1998.
- Biswas, C., and H. Na., Multisource volumetric tomography for over-the-horizon radar, *Radio Sci.*, 33(6), 1685-1703, 1998.
- Davis, K., *Ionospheric Radio*, Peter Peregrinus, London, 1990.
- Kak, A. C., and M. Slaney, *Principles of Computerized Tomography*, IEEE Press, Piscataway, N. J., 1988.
- Leitinger, R., Data from Orbiting Navigation Satellites for Tomographic Reconstruction, *Int. J. Imaging Syst. Technol.*, 5(2), 86-96, 1994.
- Mitchell, C. N., S. E. Pryse, L. Kersley, and I. K. Walker, The correction for the satellite-receiver longitude difference in ionospheric tomography, *J. Atmos. Sol. Terr. Phys.*, 59(16), 2077-2087, 1997.
- Na, H., and H. Lee, Resolution degradation parameters of ionospheric tomography, *Radio Sci.*, 29(1), 115-125, 1994.

List of Figures

- Figure 1. Comparison of (a)-(b) Imaging Geometries and (c)-(d) Coverage maps between Medical and Ionospheric Tomography Systems.
- Figure 2. Definition of Coverage Parameters.
- Figure 3. Diagrammatic Representation of CIT Imaging Systems for Four Campaigns.
- Figure 4. (a) Typical Variation of Percentage Coverage With Image Resolution in Two-Dimensions (b) Explanation of Coverage Variation.
- Figure 5. Comparison of Coverage Convergence with Resolution for (a) MACE-93 and (b) Australia-95 Campaigns for $Z = 4$ of 7 Planes.
- Figure 6. Coverage Convergence With Longitudinal Resolution.
- Figure 7. (a) CIT Imaging Geometry and Coverage Map for System 1.
- Figure 7. (b) CIT Imaging Geometry and Coverage Map for System 2.
- Figure 7. (c) CIT Imaging Geometry and Coverage Map for System 3.
- Figure 7. (d) CIT Imaging Geometry and Coverage Map for System 4.
- Figure 7. (e) CIT Imaging Geometry and Coverage Map for System 5.
- Figure 8. (a) Original Test Image. (b)-(f) Reconstructions for CIT Imaging Systems of Figures 7(a)-(e).
- Figure 9. Explanation of Altitudinal Shift for Non-Coplanar Stations. (a) Narrow Angle of Information (b) Low Angle of Elevation.

List of Tables

Table 1. List of Coverage Parameters.

Table 2. Chart of Geographic Distances and Image Resolutions for Geocentric Coordinate System.

Table 3. Results of Percentage Coverage Versus Resolution Analysis on Four Experimental CIT Imaging Systems.

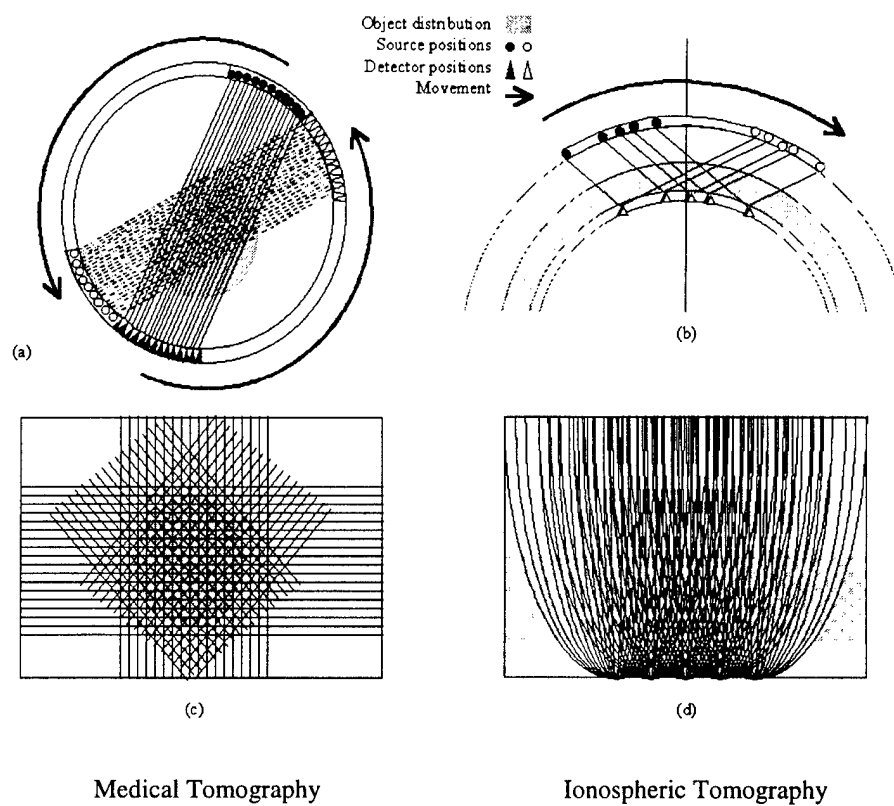


Figure 1. Comparison of (a)-(b) Imaging Geometries and (c)-(d) Coverage maps between Medical and Ionospheric Tomography Systems.

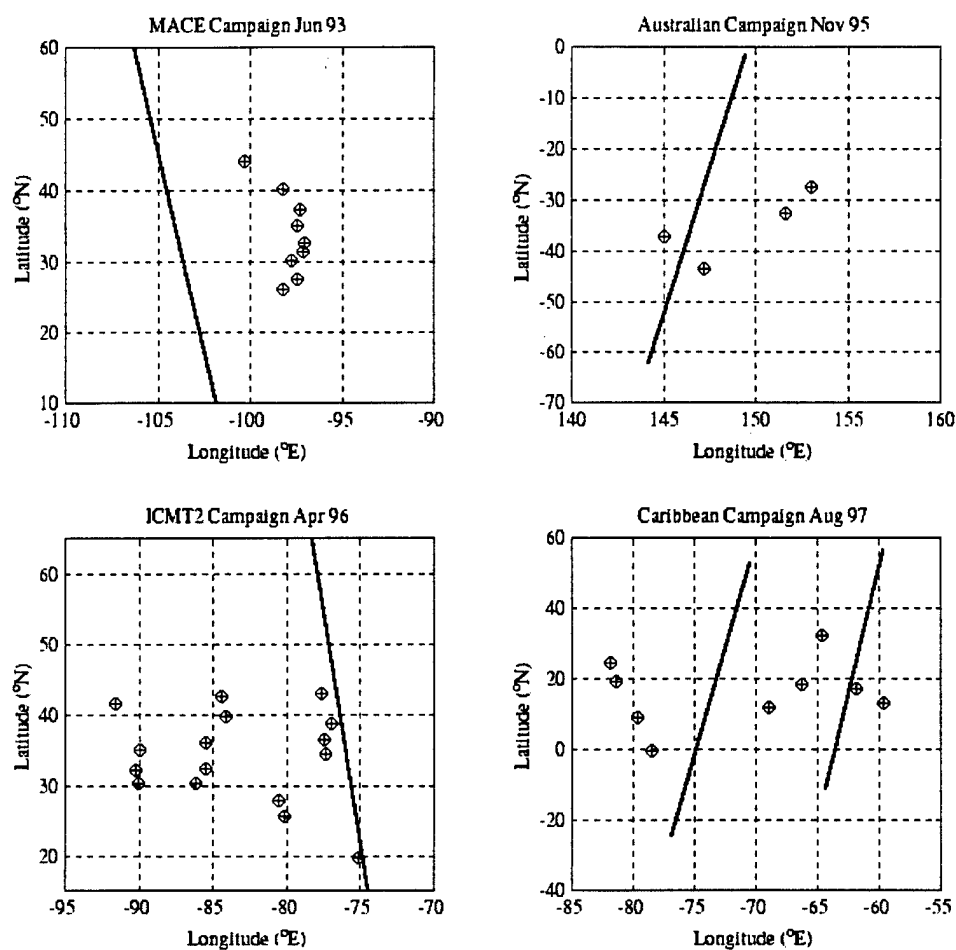
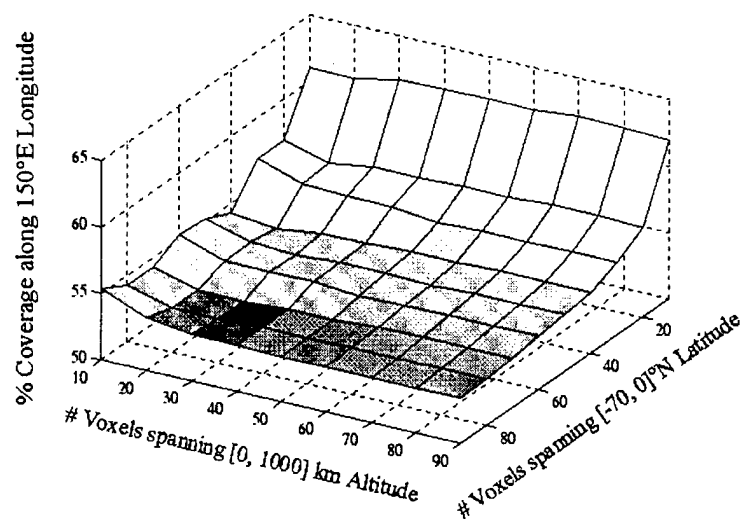
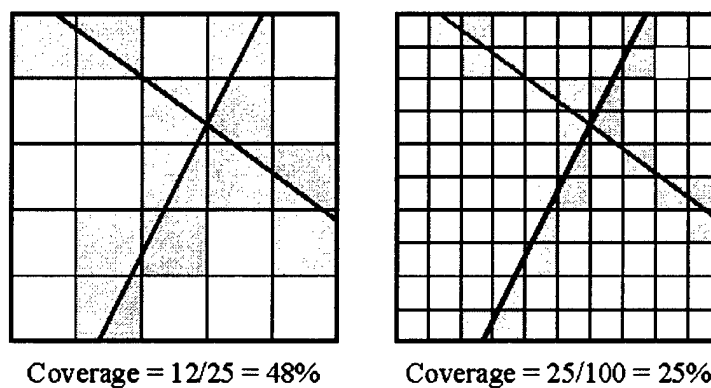


Figure 3. Diagrammatic Representation of CIT Imaging Systems for Four Campaigns.



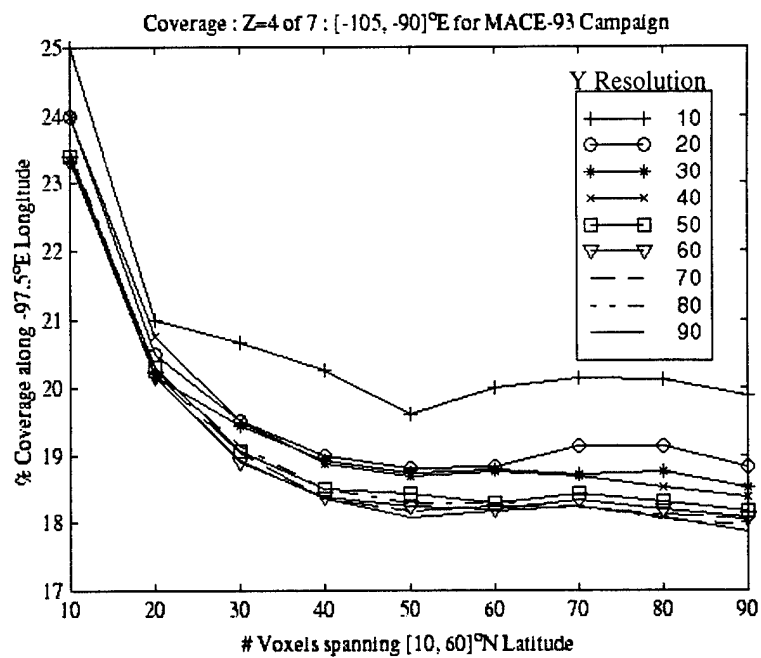
(a)

Measure of Preliminary Coverage

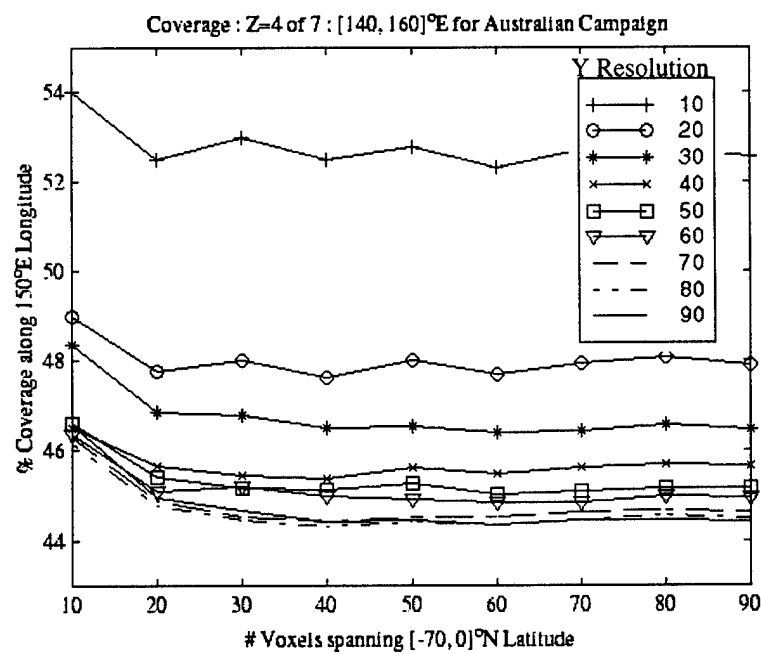


(b)

Figure 4. (a) Typical Variation of Percentage Coverage With Image Resolution in Two-Dimensions (b) Explanation of Coverage Variation.



(a)



(b)

Figure 5. Comparison of Coverage Convergence with Resolution for (a) MACE-93 and (b) Australia-95 Campaigns for Z = 4 of 7 Planes.

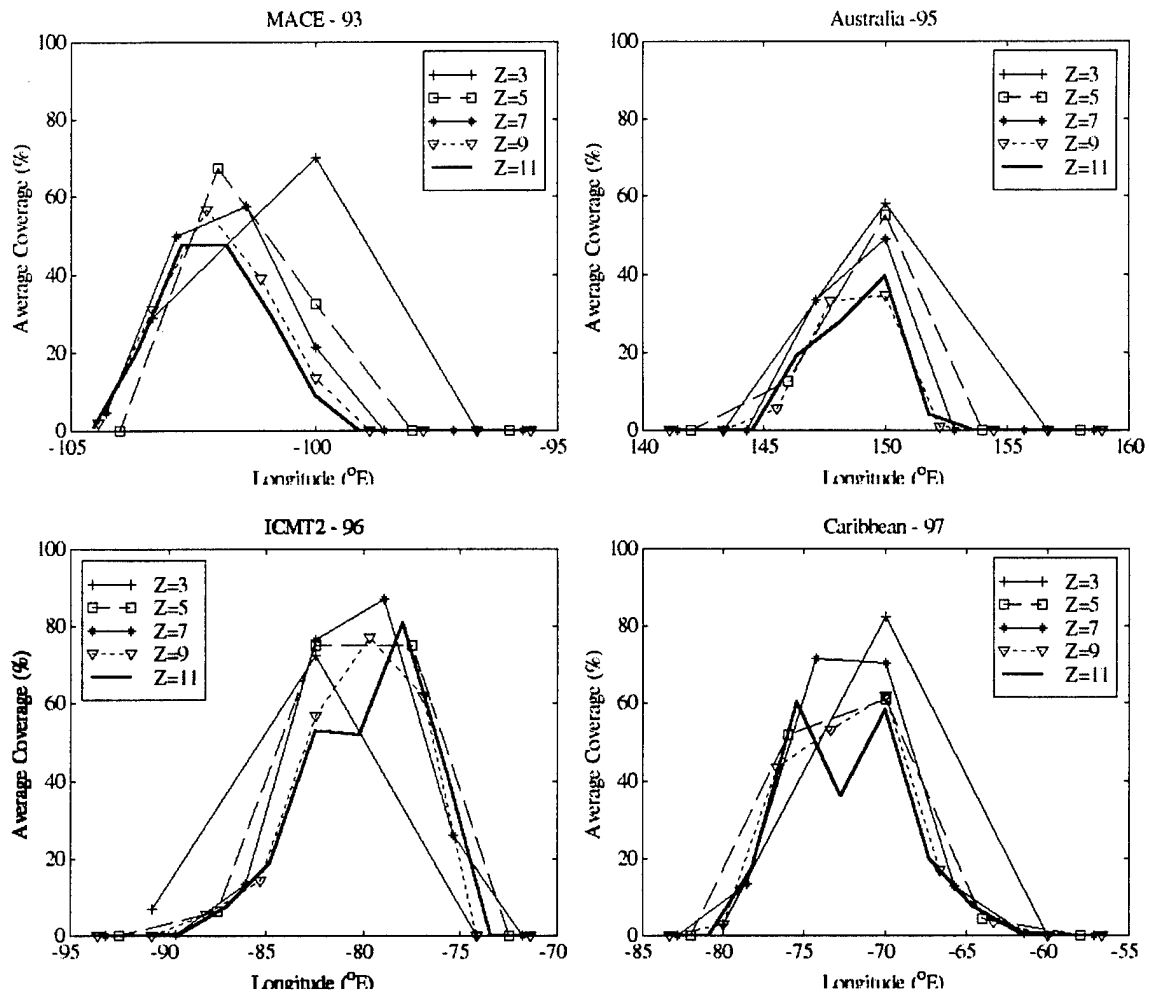


Figure 6. Coverage Convergence With Longitudinal Resolution.

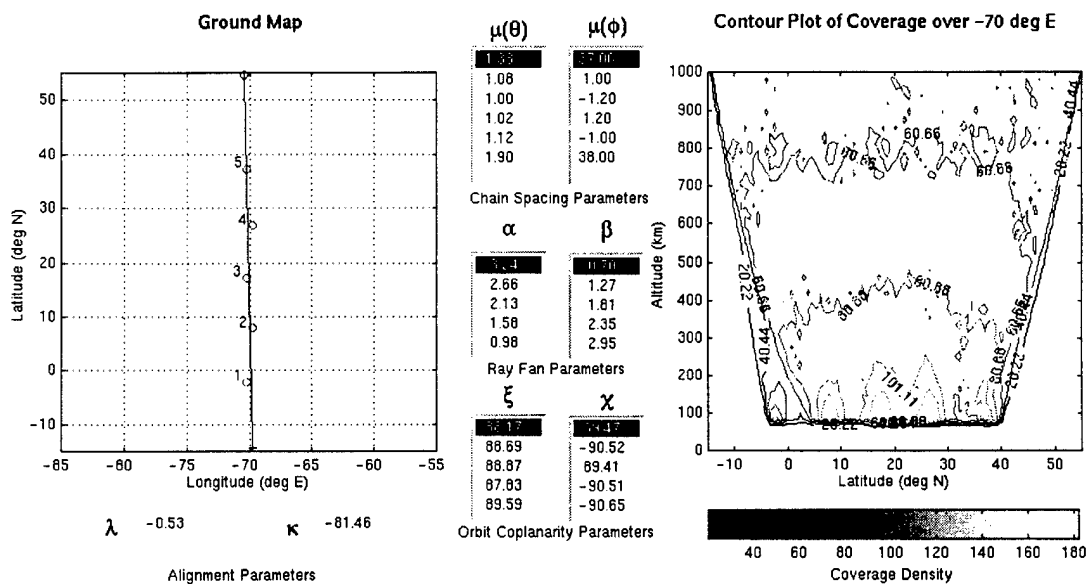
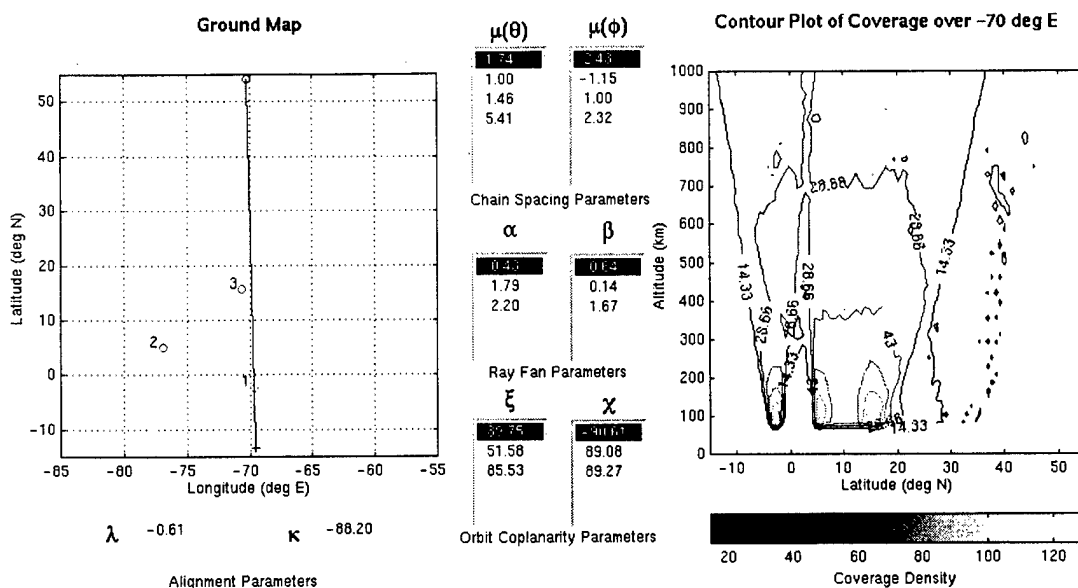
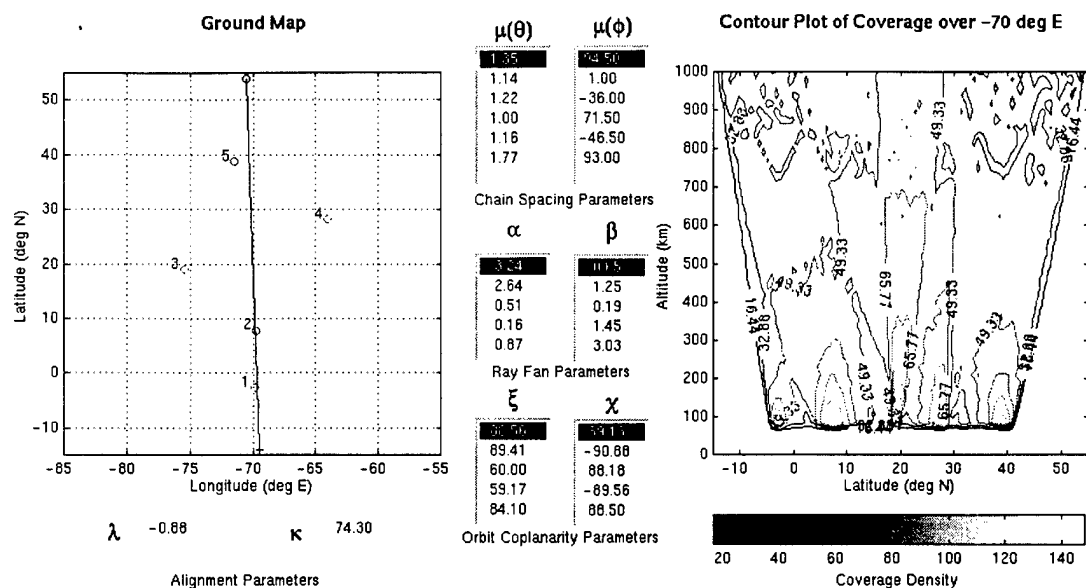


Figure 7. (a) CIT Imaging Geometry and Coverage Map for System 1.





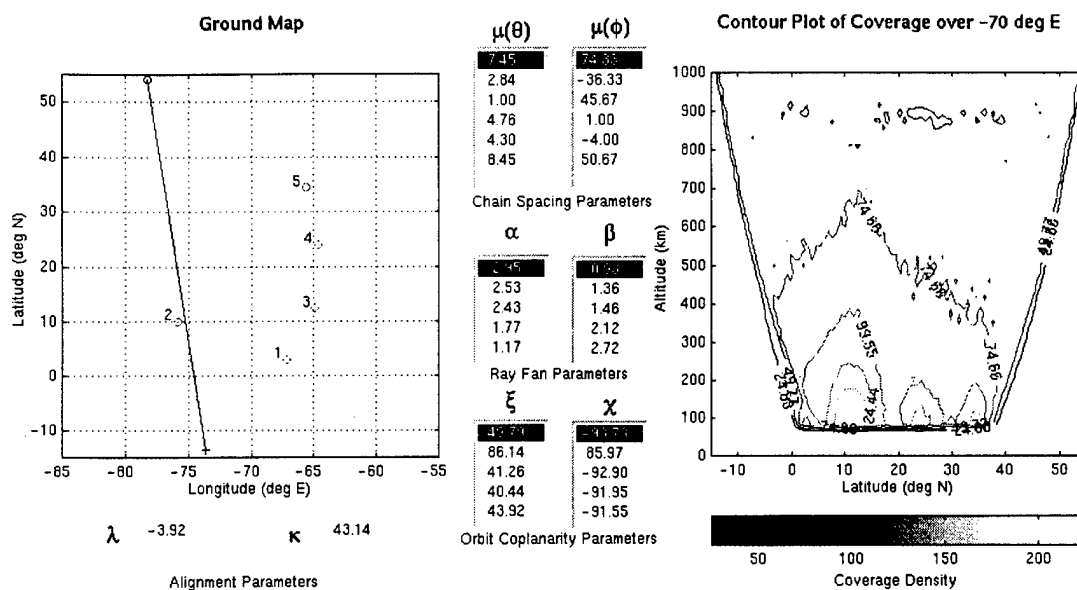


Figure 7. (e) CIT Imaging Geometry and Coverage Map for System 5.

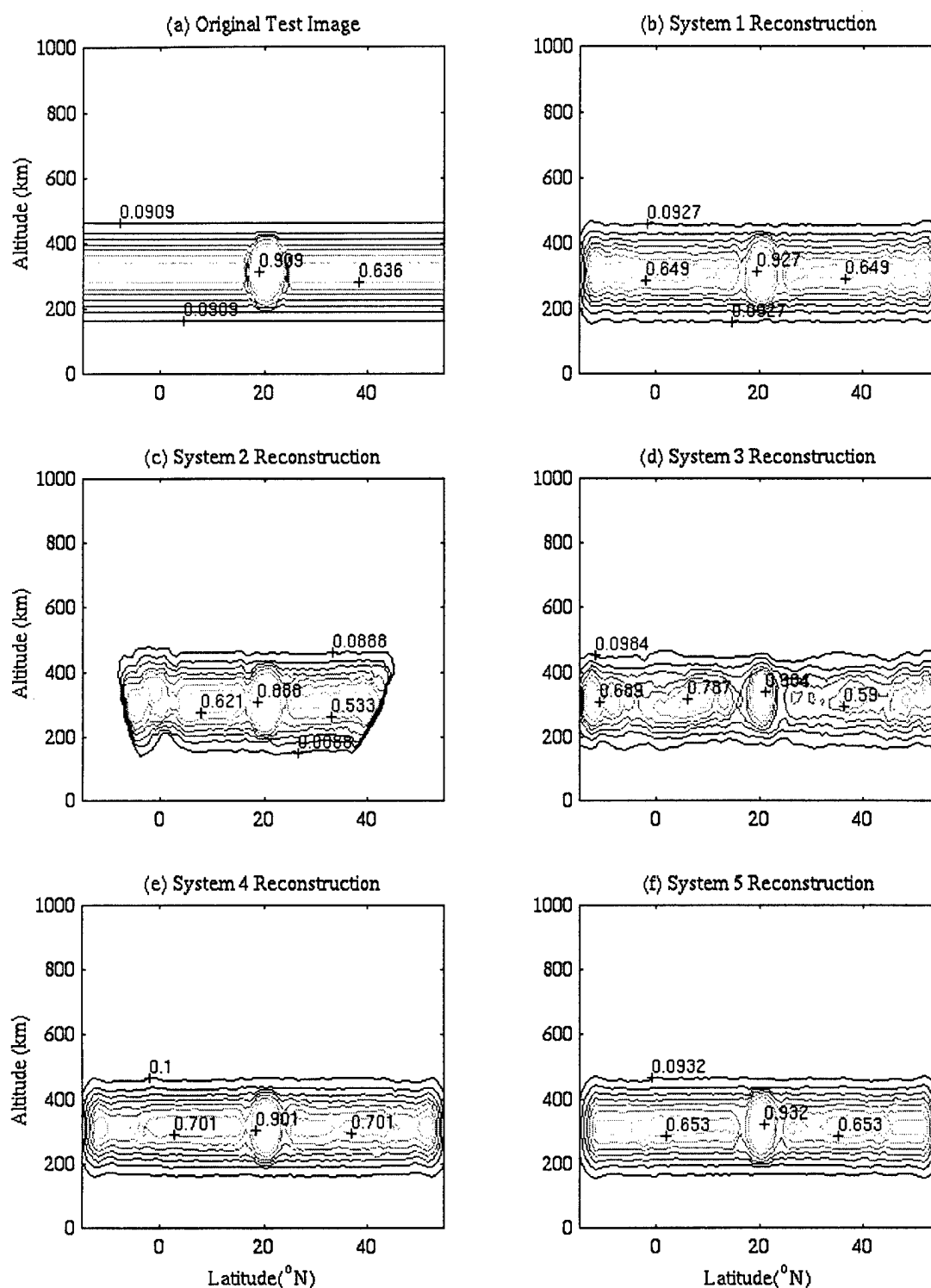


Figure 8. (a) Original Test Image. (b)-(f) Reconstructions for CIT Imaging Systems of Figures 7(a)-(e).

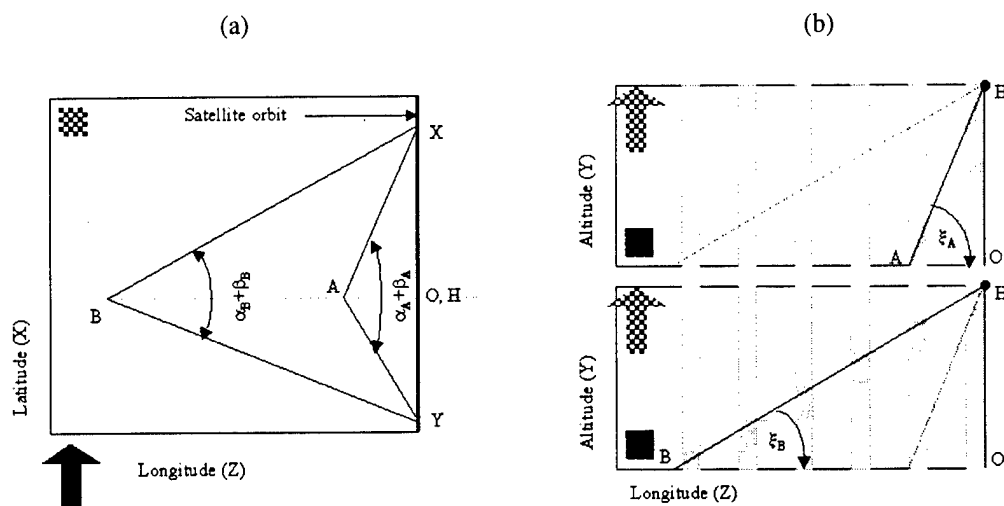


Figure 9. Explanation of Altitudinal Shift for Non-Coplanar Stations. (a) Narrow Angle of Information (b) Low Angle of Elevation.

Coverage Parameter	Symbol	Type	Definition
Orbit disparity	λ	SOP	Angular divergence of satellite orbit from center longitude
North angular fan	α_x	SOP	Angular coverage to the north from station x
South angular fan	β_x	SOP	Angular coverage to the south from station x
Fan balance	ν_x	SOP	$= (\alpha_x - \beta_x) / (\alpha_x + \beta_x)$
Chain disparity	κ	GSP	Angular divergence of chain from center longitude
Latitudinal Spacing	μ_θ	GSP	Vector of receiver spacing in north-south direction
Longitudinal Spacing	μ_ϕ	GSP	Vector of receiver spacing in east-west direction
Orbit elevation	ξ_x	GSP	Elevation of nearest point on orbit w.r.t. station x
Orbit azimuth	χ_x	GSP	Azimuth of nearest point on orbit w.r.t. station x
Directional matrix	Δ	GSP	$[\xi_1, \chi_1 ; \xi_2, \chi_2 ; \dots ; \xi_n, \chi_n]$

Table 1. List of Coverage Parameters.

# Voxels	MACE-93, ICMT2-96		Australia - 95		Caribbean - 97	
	[10, 60] °N, [15, 65] °N		[-70, 0] °N		[-10, 55] °N	
	° Latitude /voxel	Earth-Dist (km) along X per voxel	° Latitude /voxel	Earth-Dist (km) along X per voxel	° Latitude /voxel	Earth-Dist (km) along X per voxel
10	5.000	555.0	7.000	777.0	6.000	666.0
20	2.500	277.5	3.500	388.5	3.000	333.0
30	1.667	185.0	2.333	258.9	2.000	222.0
40	1.250	138.8	1.750	194.3	1.500	166.5
50	1.000	111.0	1.400	155.4	1.200	133.2
60	0.833	92.5	1.160	129.5	1.000	111.0
70	0.710	79.3	1.000	111.0	0.857	95.1
80	0.625	69.4	0.875	97.1	0.750	83.3
90	0.555	61.7	0.777	86.3	0.667	73.9

(a) Latitudinal Resolution.

# Voxels	Altitudinal Resolution (km)
	[0, 1000] km
10	100.0
20	50.0
30	33.3
40	25.0
50	20.0
60	16.7
70	14.3
80	12.5
90	11.1

(b) Altitudinal Resolution.

# of Z plane	MACE-93			Australia-95			ICMT2-96			Caribbean-97		
	[-105, -90]°E			[140, 160]°E			[-95, -70]°E			[-85, -55]°E		
	° / Z	Distance (km)		° / Z	Distance (km)		° / Z	Distance (km)		° / Z	Distance (km)	
		N [†]	S [†]		N [†]	S [†]		N [†]	S [†]		N [†]	S [†]
3	5.00	278.3	548.1	6.67	742.5	253.9	8.33	391.9	895.7	10.00	638.5	1096.3
5	3.00	167.0	328.9	4.00	445.3	152.3	5.00	235.2	537.6	6.00	383.1	657.8
7	2.14	119.1	234.6	2.86	318.4	108.9	3.57	167.9	383.9	4.29	273.9	470.3
9	1.67	92.9	183.1	2.22	247.1	84.5	2.78	130.8	298.9	3.33	212.6	365.1
11	1.36	75.7	149.1	1.82	202.6	69.3	2.27	106.8	244.1	2.27	144.9	248.9

† Longitudinal Resolutions at the North (N) and South (S) ends of the view volume are indicated.

(c) Longitudinal Resolution.

Table 2. Chart of Geographic Distances and Image Resolutions for Geocentric Coordinate System.

# Z plane	MACE-93	Australia	ICMT2	Caribbean
1 of 3	27-31	0	0-14	2-4
2 of 3	66-74	52-64	55-90	80-85
3 of 3	0	0	0	0
1 of 5	0	0	0	0
2 of 5	65 - 70	c	4-9	48-56
3 of 5	30-35	50-60	72-78	56-66
4 of 5	0	0	83-87	3-6
5 of 5	0	0	0	0
1 of 7	3.5-6	0	0	0
2 of 7	53-47	0	0-0.5	10-17
3 of 7	63-52	27-40	11-16	68-75
4 of 7	25-18	44-54	67-76	67-74
5 of 7	0	0	86-88	10-16
6 of 7	0	0	25-27	0-1
7 of 7	0	0	0	0
1 of 9	1.4-2.8	0	0	0
2 of 9	29-33	0	0	2-4
3 of 9	52-61	3-8	2-6	44-53
4 of 9	35-43	28-38	12-17	48-58
5 of 9	11-16	39-48	52-62	58-66
6 of 9	0	0.5-2	74-80	14-20
7 of 9	0	0	59-65	2-5
8 of 9	0	0	0	0
9 of 9	0	0	0	0
1 of 11	0.5-2	0	0	0
2 of 11	18-23	0	0	0
3 of 11	43-52	0	0-1	14-21
4 of 11	42-53	12-26	6.5-9	56-65
5 of 11	27-33	23-33	15-23	31-41
6 of 11	7-11	35-44	48-58	54-63
7 of 11	0	2-6	54-61	16-24
8 of 11	0	0	78-85	5-10
9 of 11	0	0	40-44	0-2
10 of 11	0	0	0	0
11 of 11	0	0	0	0

Table 3. Results of Percentage Coverage Versus Resolution Analysis on Four Experimental CIT Imaging Systems.

Techniques for evaluation and analysis of ionospheric images

Chaitali Biswas and Helen Na

Department of Electrical Engineering

University of California, Los Angeles

Abstract

This paper introduces a quantitative feature extraction technique for the evaluation of the content and the quality of images of ionospheric electron distribution. Parametric alteration of the properties of image histograms of electron density distributions enable the separation of features such as enhancements, depletions and small scale irregularities of such images from the background. This technique is aimed at providing comparison of plasma images obtained from different sources and for the utilization of the image information content for various applications in real time.

1. Introduction

Recent advances in ionospheric probing and imaging techniques and in the development of various applications which utilize images of ionospheric electron density distribution in real-time indicate the need for a simple, automatic, unbiased and universally applicable numerical method for evaluating the contents of such images. Two and three dimensional maps of ionospheric electron density are obtained from various sources ranging from extrapolated distribution profiles from HF ionosondes [Davies, 1990; Hausman and Nickisch, 1998], to true images generated by ionospheric tomography using VHF and UHF signals [Austen *et al.*, 1988; Fremouw, 1992; Na and Lee, 1994; Raymund, 1994; Fougere, 1995; Na and Biswas, 1996; Sutton and Na, 1996; Biswas and Na, 1998a; Fehmers, 1998; Kulinski, 1998] and even more accurate images mapped by incoherent scatter radars [Hunsucker, 1991]. The geographical extents of these images can vary from very localized areas in the vicinity of quasi-vertical ionosondes to several thousands of kilometers below a satellite orbit or along the look directions of an oblique backscatter sounder. The resolution and reliability of the actual pixel based information content in these electron density maps vary significantly based on the accuracy of measurement and on image reconstruction techniques. In addition, the information content of a given image is defined by the applications that make use of various measurements from the distribution map.

Current literature on ionospheric imaging indicates the need for a simple and unbiased numerical method for evaluating the quality of reconstructed images which is suitable for diverse applications. Images obtained by computerized ionospheric tomography (CIT) have traditionally been subjected to visual evaluation and analysis. Comparison of CIT reconstructions with images obtained from incoherent scatter radar (ISR), which is regarded as the best process of estimating

reconstruction quality, would also benefit from the use of an abstract quantitative analysis technique. Often, various CIT reconstructions are compared to each other for algorithm evaluation. This situation emphasizes the need for an analysis procedure that is independent of the source of the image distribution and is capable of comparing image information at a more abstract level in a manner similar to that of a human expert.

Image reconstruction for CIT requires the simultaneous participation of a broad spectrum of disciplines ranging from the digital domain of image processing to that of plasma physics involving parametric equations, which, for all practical purposes, can be considered to be functions of continuous space and time domains. The final image produced by a generic CIT algorithm could be the result of statistical analysis, iterative algebraic tomographic reconstruction, basis function decomposition, physical constraint based optimization or various combinations of the above. In addition, the scale of the image and location of the CIT system play a significant role in determining contrast, resolution and several other visible attributes of features within the image. Consequently, the list of image differences at the pixel level or even at that of regional texture is often too exhaustive for enumeration and consideration as a basis for quantitative image analysis. Various real time applications such as over-the-horizon radar (OTHR) require specific information from images of ionospheric plasma distribution such as the height and electron content of maximum electron density [*Biswas and Na, 1998b*]. Pixel based comparative processing throughout the image plane such as square error estimation would involve unnecessary computation when all that is required is the mutual comparison of a set of one-dimensional profiles from a large number of competing reconstructions. Abstraction of an image using feature extraction and classification techniques can provide robust compaction of information while

providing a scheme for application dependent quality estimation. It must be emphasized however, that standard image comparison schemes such as mean square error images and image gradient differentials carry vital information regarding image quality and must not be completely disregarded in the analysis process.

The aim of this paper is to introduce methods of extracting relevant information from competing images as well as the differentials of their pixel based attributes for quantitative evaluation of quality. The next section discusses the major properties of a typical image of ionospheric plasma and distribution features of interest to major applications such as OTHR or HF communications systems. Section three introduces the processes of parametric histogram distribution (PHD) and subsequent feature extraction. The following section involves a discussion of various methods of image-plane based comparison of plasma images which can provide direct measurement of several significant changes during real-time monitoring of ionospheric structures. Section five summarizes the need, the approach and the significance of the newly developed image content and comparison technique and discusses issues associated with future developments in this area of research.

2. Features of Interest in Ionospheric Electron Density Images

The first step in the information extraction from a signal for abstract representation involves the selection of features, which provide robust, yet reliable accounts of its vital attributes. Information about the nature of commonly encountered ionospheric features was obtained from various sources ranging from direct and reliable measurements using incoherent scatter radar (ISR) to images generated by empirical atmospheric plasma models such as the International Reference Ionosphere (IRI) and the Parameterized Ionospheric Model (PIM).

The simplest model of the ionosphere is that of a horizontally stratified, spherical shell surrounding the earth at between of approximately 100-450 km. The altitudinal variation of density can be approximated to an asymmetric Gaussian or an alpha-Chapman profile [Davies, 1990] with the sharper gradient below the height of maximum electron density. Observed in a two-dimensional ground-altitude plane, the section of this shell appears to be a horizontal band as shown in Figure 1. Embedded within the band are regional enhancements of extremely high electron content known as peaks caused by plasma convection in the vicinity of the magnetic equator or due to sudden electromagnetic disturbances such as solar storms in the auroral regions. The size, shape and density of these peaks vary with location, time and ambient heliogeomagnetic activity. The presence of such embedded peaks contributes to significant horizontal gradients in the surrounding band. Isolated patches of equally high density but significantly smaller dimensions occur as sporadic E and F_2 formations that drift through the ionospheric matrix due to gradients in plasma density between the sunlit and dark portions of the upper atmosphere. Although smaller in size and lasting for shorter durations than the peaks, these patches are of vital importance to communications systems since they result in fading and radio scintillation. Thus the band, the peak and the patch were selected as the three most important features of an image of ionospheric electron density.

Another attribute of importance in an ionospheric image is the profile of maximum electron density. This can be viewed as a surface in the three dimensional spatial co-ordinate system of latitude, longitude and altitude indicating the geographic location with the color of a point on the surface serving as the fourth dimension indicating the maximum electron density. For conventional two-dimensional CIT images with the altitude versus latitude co-ordinate system,

the maximum density plane reduces to a curve in three dimensions with electron density serving as the third axis. Examples of the latter convention are shown in Figure 2, where the three composite plots represent three longitudinal planes of three IRI-90 images. Each composite plot shows the variation of $N_{\max}(F_2)$ against the latitude and the altitude $h_{\max}(F_2)$ in the three images for a single longitudinal plane.

In addition, pixel based image differences such as squared errors between two images and their normalized versions provide important information regarding the recovery of absolute and relative electron density values within the image plane. The most important information that can be extracted from square error plots are occurrences of isolated pockets of high error such as caused by relative spatial shift of features between two reconstructions or a reconstruction and an ISR image. The indeterminate nature of the shape, extent and magnitudes of these regions make it difficult to classify them into much beyond pockets of magnitude and shape errors. Comparison of corresponding pockets in the mean square and normalized mean square error images, however yields information regarding the efficiency of value recovery in the region versus shape recovery given identical conditions of coverage and image reconstruction procedure. This will help distinguish between procedures that emphasize value recovery in localized regions from those which enforce recovery of the shape of plasma distributions.

Several applications such as ROTH, require information about local gradients in ionospheric images. Differences, in both the magnitude and angular components of gradient images obtained from two different sources, highlight the relative susceptibility of the inversion schemes to discontinuities in coverage. As with mean square error images, the principal

information carried by gradient differential images lie in the existence and magnitude of high error regions, which can be termed as slope pockets.

Features chosen for image representation and comparison as described in above are enlisted along with suitable attributes in Table 1. For bands, peaks and pockets, their considerable extent with respect to the image area make them eligible for boundary detection, calculation of geometric *centroids* and value-centroids or *valtroids*, and the length and orientation of the major axis in the Cartesian co-ordinate system. For small scale but significant structures such as patches, the major attributes for classification are location and density. The second column of Table 1 refers to the base image from which the feature is extracted. The abbreviations “ase” and “nse” stand for “absolute squared error” and “normalized square error” images, whereas “abgrme” and “abgrae” stand for “absolute gradient magnitude error” and “absolute gradient angular error” images respectively.

3. Feature Extraction Procedure for CIT Images

Feature extraction for bands and peaks was performed using separate intensity reassignment procedures for the histogram of a given ionospheric image. The examples of ionospheric histograms in Figure 3, show the presence of a significant background mode followed by a relatively low uniform ledge representing the foreground with most of the electron content. The aim of the histogram reassignment processes is to separate the foreground part of the histogram into two separate entities, the band and the peaks within it. The image processing technique for achieving uniformity in histogram profile is termed equalization. Therefore the reverse procedure of separating a uniform histogram into one or more distinctive modes can be termed unequalization. Contrary to the closed form definition of histogram equalization where the

goal is to achieve a uniform histogram density for all intensities, this reverse process requires parametric specifications for controlling the position of occurrence and extent to which mode separation is permitted. The parametric histogram distribution (PHD) approach developed for ionospheric images involves a three-path process which simultaneously separates the band, the peaks and the patches from the background information.

The first step in the detection of bands and peaks is the definition of an intensity transformation function. In the case of histogram processing for peak detection, it was necessary to separate the original histogram into two distinct modes, that of the peak(s) and that of everything of lesser intensity. This was achieved by a space translated single term polynomial of the form:

$$v = (u - 0.5 + \varepsilon)^{-\gamma} + 0.5 \quad (1)$$

Here u and v represent the normalized axes of the original and the transformed histogram intensities respectively. Figure 4a shows the nature of the above curve where, for all practical purposes, $-0.5 < \varepsilon < 0.5$, and $1 < \gamma < 9$. The parameter γ represents the degree of contrast enforced between the peaks and the rest of the image, whereas ε represents the threshold intensity at which the contrast is centered. Figure 4b shows the curve representing histogram transformation for isolation of the band. The aim is to separate the histogram into three principal modes representing the background, the band and the peaks while maintaining a uniform intensity within each mode. The equation for the curve shown in Figure 4b is:

$$v = \begin{cases} 0.5(2u)^\delta & u \in [0.00, 0.25] \\ 0.5(2u - 1)^\delta & u \in [0.25, 0.75] \\ 0.5(2u - 2)^\delta & u \in [0.75, 1.00] \end{cases} \quad (2)$$

The curve parameter δ has a value in the range [1, 9]. Figure 5 shows an original ionospheric image and the result following histogram redistribution.

The second step in feature extraction is intermodal boundary detection. Both the transformed histograms shown in Figure 5 have irregular profiles with several subsidiary peaks and valleys in each principal mode. An established natural method of threshold detection is iterative nodal propagation [Biswas, 1993] where all the discrete intensities of the histogram act as nodes in a neural network. The network is fired by initiating a nearest neighbor propagation and feedback sequence simultaneously from each peak. The iterative process results in modification of the histogram profile by accumulating the contents of arbitrarily located neighboring modes under the principal modes and smoothening out the profile. This process is continued for both the peak and band histograms until two and three modes remain in them respectively. The intermodal valleys denote modal thresholds. Figure 6 shows the flowchart for the computation of threshold and an example of progressive modal thresholding.

The third and final stage of the feature extraction process is the detection of features within the boundary images and calculating vital attributes of each. Boundary detection is performed using an 8-way directionality map [Gonzalez and Woods, 1993]. Detection of false features is minimized by only permitting those with greater than a certain number of boundary elements to be registered, based on the geographical dimensions of the voxels. Figure 7 shows the boundary images of the peak and band images shown in Figure 5.

Following peak and band extraction, three important sets of attributes are calculated for each. They are the positions of the geometric and the value density centroids [G_x , G_y] and [V_x , V_y] and the length and orientation of the major axis [M_a , M_o]. Given a boundary defined as the

ordered and directed set of points, $\mathbf{B} = \{(x_1, y_1), (x_2, y_2), \dots, (x_n, y_n)\}$ and the original image $\mathbf{P} = \{p(x_i, y_i)\}$, the centroids are defined as follows:

$$[G_x, G_y] = \frac{1}{n} \left[\sum_{i=1}^n x_i, \sum_{i=1}^n y_i \right] \quad (3)$$

$$[V_x, V_y] = \frac{1}{\sum_{i=1}^n p(x_i, y_i)} \left[\sum_{i=1}^n x_i p(x_i, y_i) + \sum_{i=1}^n y_i p(x_i, y_i) \right] \quad i \in \text{Feature} \quad (4)$$

The length and orientation of the major axis of the feature are defined using conventional Cartesian coordinates, where given the end points $[a_x, a_y]$ and $[b_x, b_y]$, the major axis vector is defined as:

$$[M_a, M_o] = [\sqrt{(a_x - b_x)^2 + (a_y - b_y)^2}, \quad 90/\pi * \tan^{-1}((a_y - b_y)/(a_x - b_x))] \quad (5)$$

Effectively, these three vectors serve as the coordinates of a six dimensional feature space where each feature F_j is represented by the sextuplet: $F_j = [G_{xj}, G_{yj}, V_{xj}, V_{yj}, M_{aj}, M_{oj}]$. Thus \mathbf{F} can be defined as the domain of the primary feature space of the contents of the original image. Figure 8 shows the set of feature attributes calculated using the parametric histogram distribution technique for the two images of Figure 3.

4. Auxiliary Differential Measurements for Image Comparison

The feature extraction process can be extended to the realm of differentials such as root square error and gradient magnitude and gradient angle images. As summarized in Table 1, the purpose of analyzing the root mean square error image resulting from two corresponding ionospheric distributions, is to identify regions and magnitudes of differences in absolute value. Feature extraction from the error images results in compaction of important information such as

the location, extent and magnitude of differences between the two images. The features obtained from various error maps such as those between an ISR image and CIT reconstructions using various algorithms, can then be compared on a quantitatively abstract basis to see which algorithm truly succeeded in incurring fewer artifacts and achieving good reconstruction. Figure 9 shows the important differential images associated the two ionospheric images of Figure 3.

The raw square difference image shows the actual degree of mismatch in electron density between two images and is useful for a direct comparison of image values. This is useful when comparing a reconstruction with a standard such as ISR image or even two different reconstructions derived from the same TEC data using different parameters or algorithmic approaches. A finer analysis of the success of each reconstruction requires comparison of the relative accuracy of feature recovery in each image. Instead of comparing actual electron density values, it is necessary to compress the dynamic range of each image to lie within the normalized range $[0, 1]$ in order to be able to detect relative recovery of features within the image plane. The principal use of the normalized square difference image is to identify the strengths and weaknesses in the reconstruction processes associated with each image in dealing with issues of non ideal system geometry and incomplete sky coverage. When one of the images is a standard, this difference measure would prove highly useful in differentiating between artifacts and valid image features. For instance, the square difference image of Figure 9a shows a substantial difference in the magnitudes of electron density over the region extending between the 50th and the 90th voxel horizontally. This prominence is not evident in the normalized difference image, which indicates that although there is a disparity between actual electron densities in that region, relative to the maximum electron densities in either, the area is of nearly identical density in both

images. If the two images were reconstructed using different methods and the maximum electron density were somewhat different in either image, Figure 9a could lead one to conclude that they were divergent representations of the actual electron density. On the other hand, Figure 9b would help reconcile the above argument because the shapes of features recovered in the inversion process would match each other even if magnitudes do not.

Differences in the gradients of two fairly similar images provide information regarding relative displacements of heights of maximum density, $h_{\max}(F_2)$, and also of the differences in the density, $N_{\max}(F_2)$, itself. Figure 9c and 9d show the magnitude and orientation of the gradient difference between the two test ionospheric images of Figure 3. According to the magnitude image of the difference in gradients, there is approximately a difference of 3 voxels in altitude in the $h_{\max}(F_2)$, between the two images for the left half of the image which eventually gets resolved in the other half. Compared to an expert judging the characteristics of electron density profile such as maximum height and gradient of the profile by directly looking at the original images, the gradient calculation approach provides one with a simple and elegant method for qualitative and quantitative evaluation of layer height and density differences between the images. The role played by the orientation image of the gradient difference is that highlighting the area of maximal gradient discrepancy between the two images. Since the vertical profile of an ionospheric image is often steeper and more dynamic than the horizontal profile, differences in orientation are likely to be expressed as horizontal lines passing through the region in between the $h_{\max}(F_2)$ s of the two images, that is at the altitude, where the difference between the skyward slope and the earthward slope of the two images is maximum. Since the orientation map tends to have a single such line of difference, given the unimodality of the vertical profile, this height can be used to diagnose the

principal region of discrepancy in the more complicated magnitude map. In addition to providing $h_{\max}(F_2)$ information, the magnitude map is also useful in locating discrepancies between horizontal inhomogeneities such as a trough between peaks. An example of this is also seen above the 14th and the 15th horizontal voxel, delineating the difference in trough locations between the two peaks as two voxels apart.

5. Conclusions

Image processing experiments were conducted on various IRI-90 images with approximately the same feature distributions and the results of feature extraction, classifications and auxiliary differential calculations. In the absence of the availability of other CIT reconstruction algorithms besides MIVIA, the comparison of different reconstructions from the same TEC data was not attempted. This was also not undertaken with the understanding that it is an entirely independent and vast area of research in itself.

The principal advantage of the parametric histogram distribution based feature extraction process to ionospheric image analysis lies in its quantitative and objective approach to defining the intensity ranges for image features. Utilization of normalized histograms ensures that the features are selected independent of actual electron density values and the process is universally applicable to all ionospheric images regardless of geographic extent, ambient ionospheric activity, method of image generation. In addition, certain image difference measures have been analyzed for the extraction of important data such as shape recovery, difference in layer heights and gradients.

Acknowledgements

This work was supported by the Office of Naval Research under grants N00014-95-0850 and N00014-97-0419 and by the National Science Foundation under grant ATM9696259.

References

- Austen, J. R., S. J. Franke, and C. H. Liu, Ionospheric imaging using computerized tomography, *Radio Sci.*, 23(3), 299-307, 1988.
- Biswas, C., *Volumetric Reconstruction for Ionospheric Tomography*, (Ph.D. Thesis), University of California, Los Angeles, 1999.
- Biswas, C., and H. Na, Three-dimensional computerized ionospheric tomography using volumetric constraints, *Radio Sci.*, 33(6), 1793-1805, 1998.
- Biswas, C., and H. Na., Multisource volumetric tomography for over-the-horizon radar, *Radio Sci.*, 33(6), 1685-1703, 1998.
- Davis, K., *Ionospheric Radio*, Peter Peregrinus, London, 1990.
- Gonzalez R. C., and R. E. Woods, *Digital Image Processing*, 1st Ed, Addison Wesley, N.Y., 1990.
- Kak, A. C., and M. Slaney, *Principles of Computerized Tomography*, IEEE Press, Piscataway, N. J., 1988.
- Leitinger, R., Data from Orbiting Navigation Satellites for Tomographic Reconstruction, *Int. J. Imaging Syst. Technol.*, 5(2), 86-96, 1994.
- Mitchell, C. N., S. E. Pryse, L. Kersley, and I. K. Walker, The correction for the satellite-receiver longitude difference in ionospheric tomography, *J. Atmos. Sol. Terr. Phys.*, 59(16), 2077-2087, 1997.
- Na, H., and H. Lee, Resolution degradation parameters of ionospheric tomography, *Radio Sci.*, 29(1), 115-125, 1994.

List of Figures

- Figure 1. Ionospheric Features of Interest.
- Figure 2. Example of Maximum F2 layer Density Profile of 3 Two-dimensional Images along (a) 70° E (b) 75° E and (c) 80° E Longitudes.
- Figure 3. Sample Ionospheric Electron Density Distributions from IRI-90 and Histograms of Number of Occurrences vs. Electron Density Values.
- Figure 4. Parametric Histogram Distribution Curves for (a) Peak and (b) Band Separation.
- Figure 5. Peak and Band Separation Using Parametric Histogram Distribution.
- Figure 6. (a) Neural Network Used for Progressive Modal Thresholding. (b) Examples of Thresholded Histograms.
- Figure 7. Boundary Detection of Peaks and Band. (b) Detection of Small Scale Disturbances.
- Figure 8. Results of Feature Extraction.
- Figure 9. Difference Images of Ionospheric Distributions Shown in Figure 3. (a) Absolute Square Difference Image (b) Normalized Square Difference Image (c) Magnitude of Gradient Error Image (d) Orientation of Gradient Error Image.

List of Tables

Table 1. Features Selected for Representing Contents of Ionospheric Images.

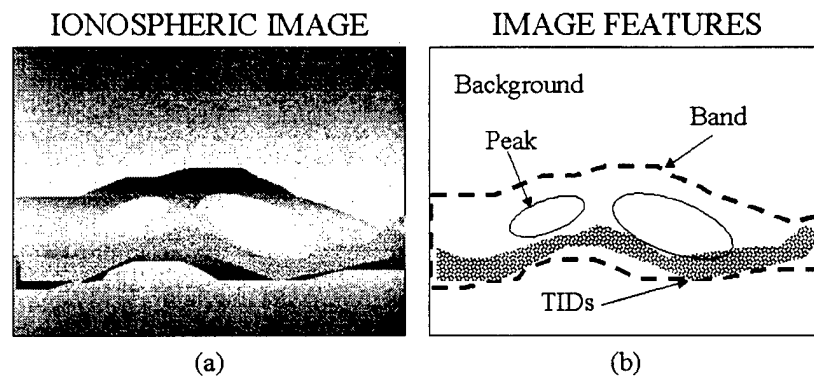


Figure 1. Ionospheric Features of Interest.

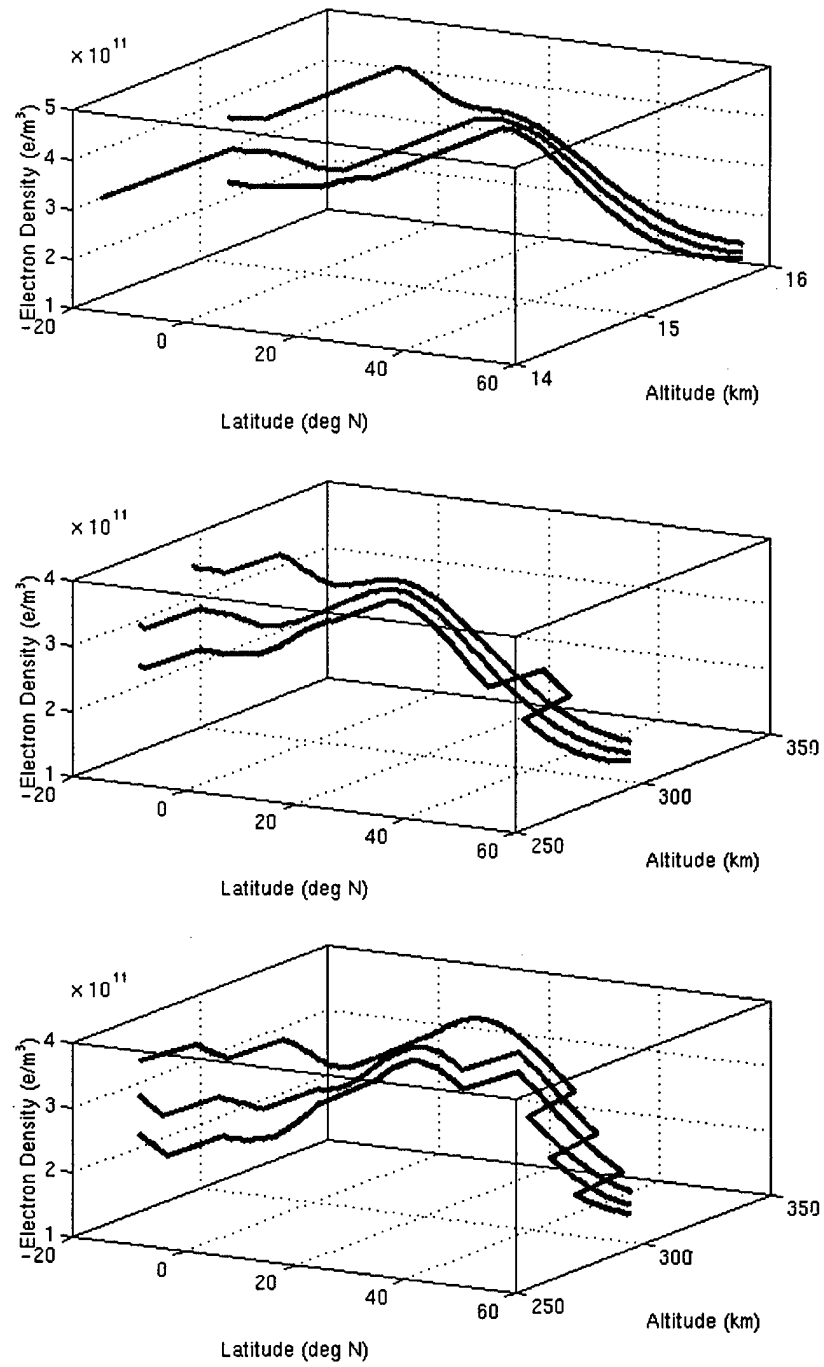


Figure 2. Example of Maximum F2 layer Density Profile of 3 Two-dimensional Images along (a) 70° E (b) 75° E and (c) 80° E Longitudes.

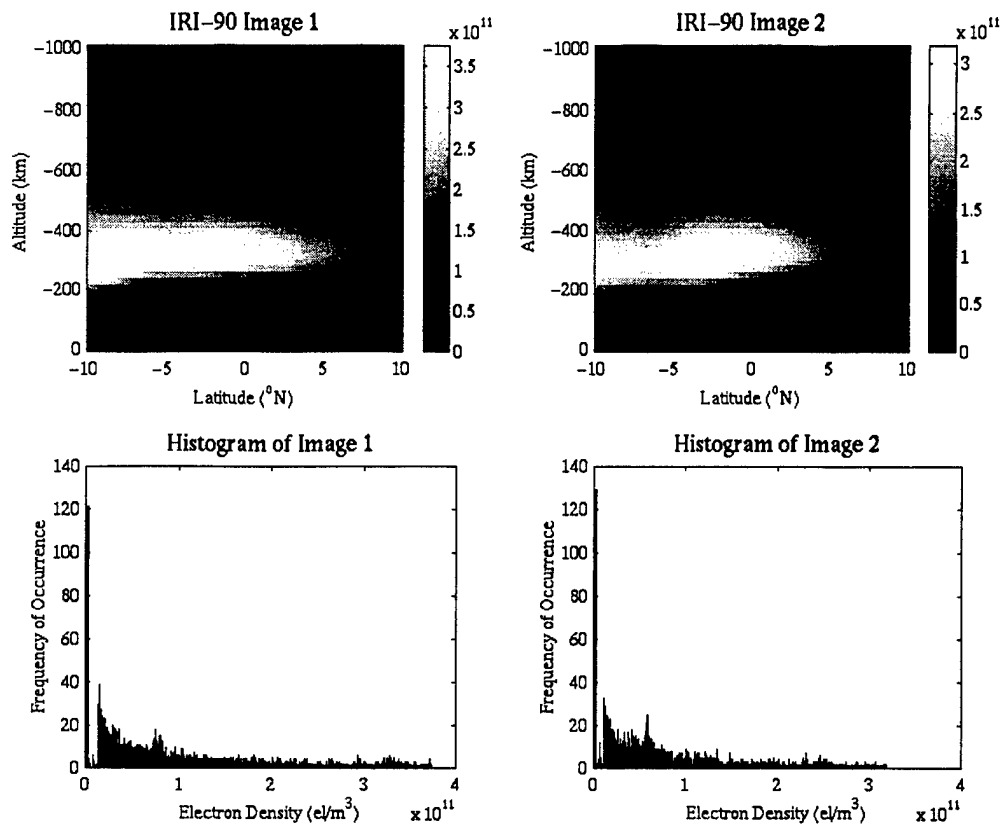


Figure 3. Sample Ionospheric Electron Density Distributions from IRI-90 and Histograms of Number of Occurrences vs. Electron Density Values.

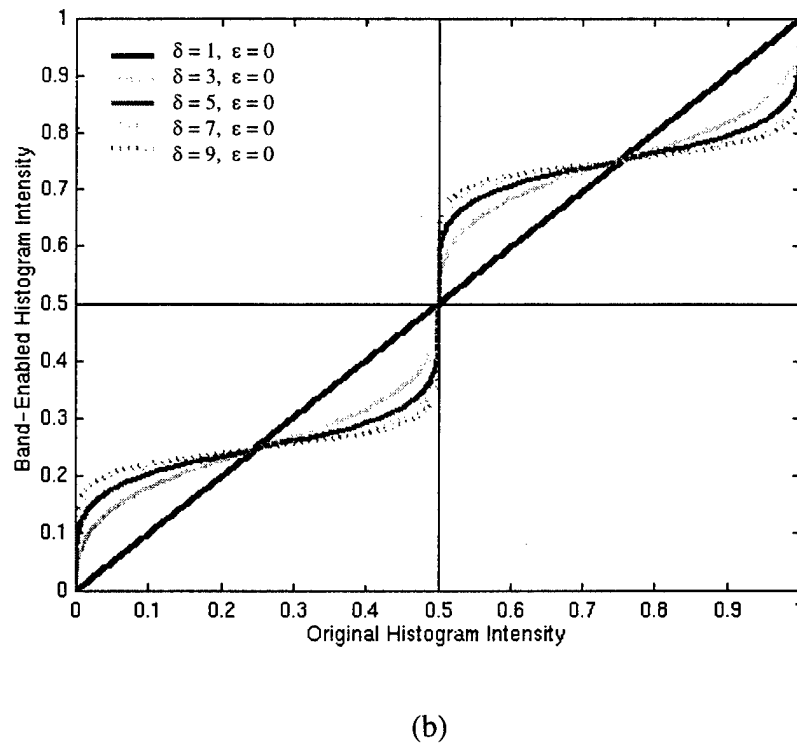
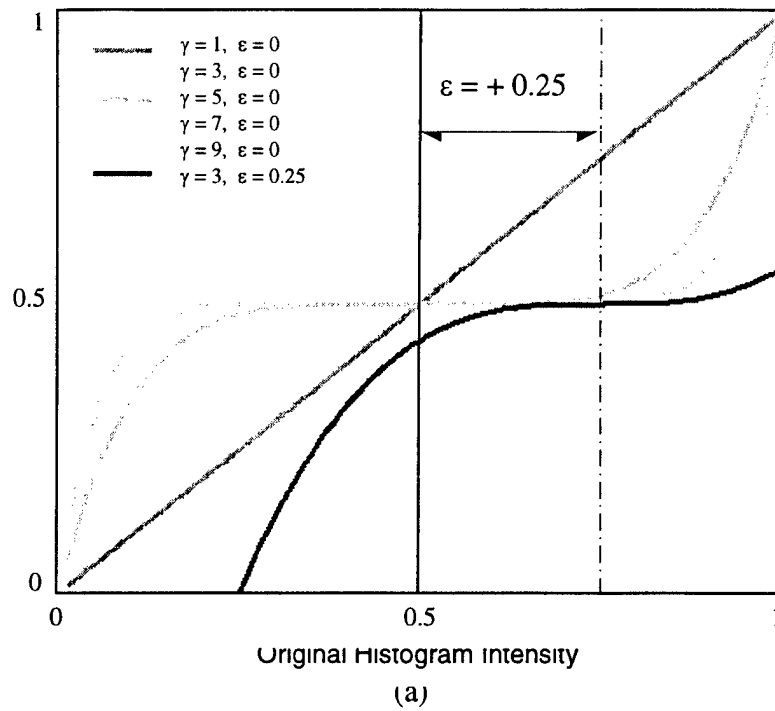


Figure 4. Parametric Histogram Distribution Curves for (a) Peak and (b) Band Separation

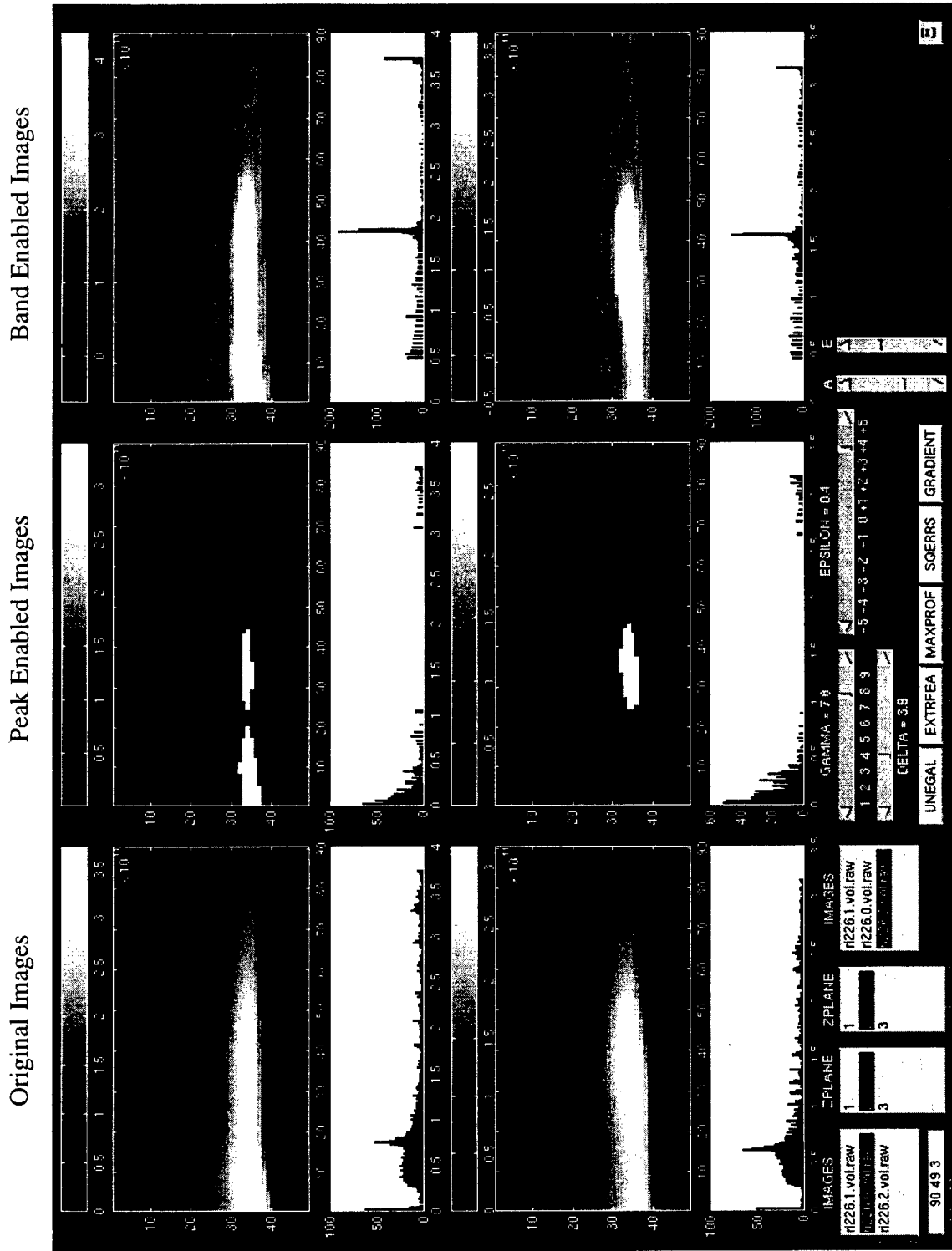


Figure 5. Peak and Band Separation Using Parametric Histogram Distribution.

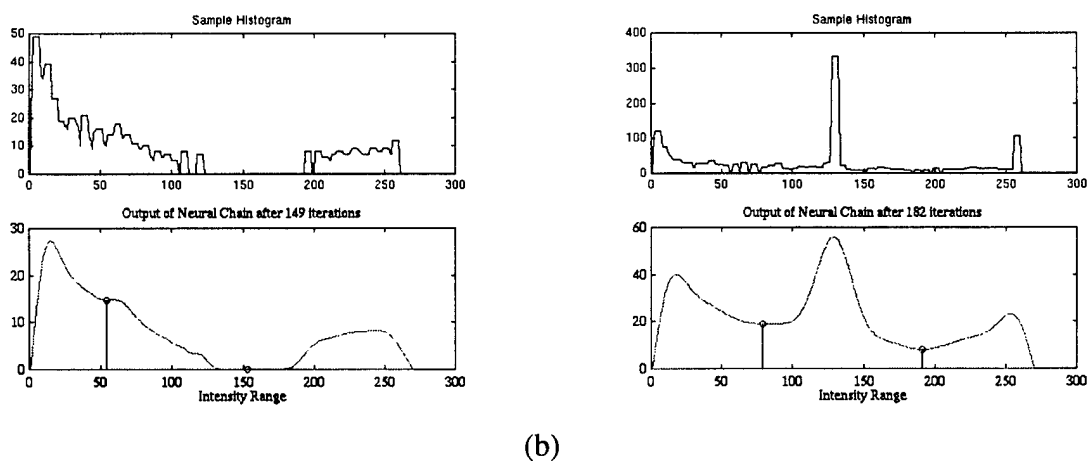
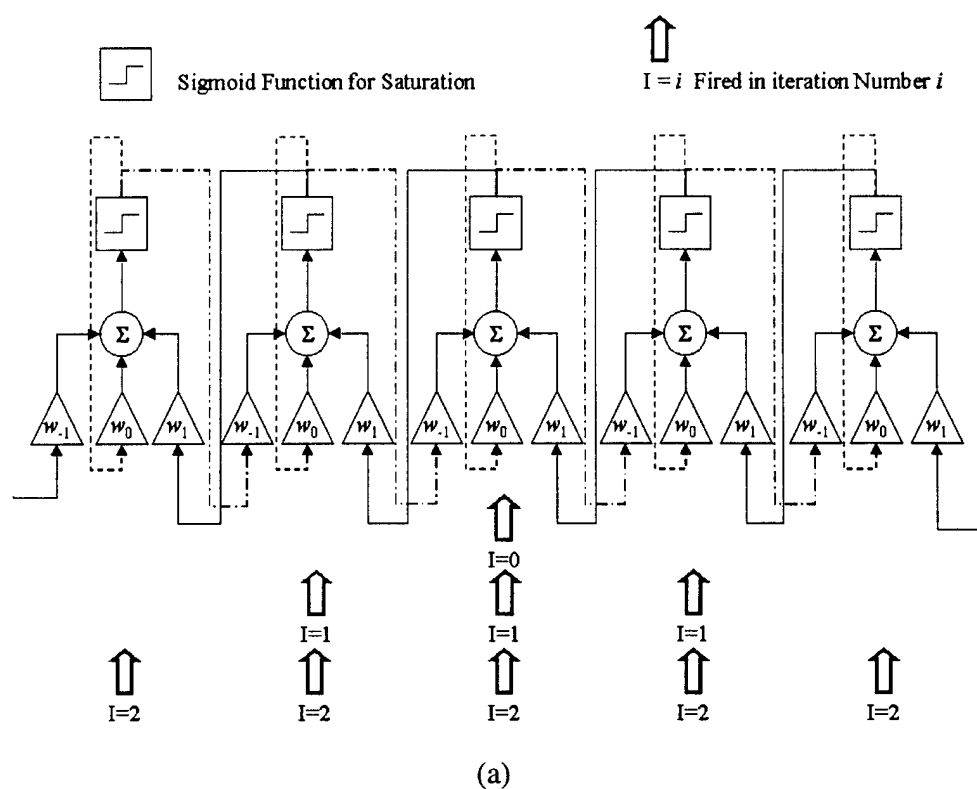


Figure 6. (a) Neural Network Used for Progressive Modal Thresholding. (b) Examples of Thresholded Histograms.

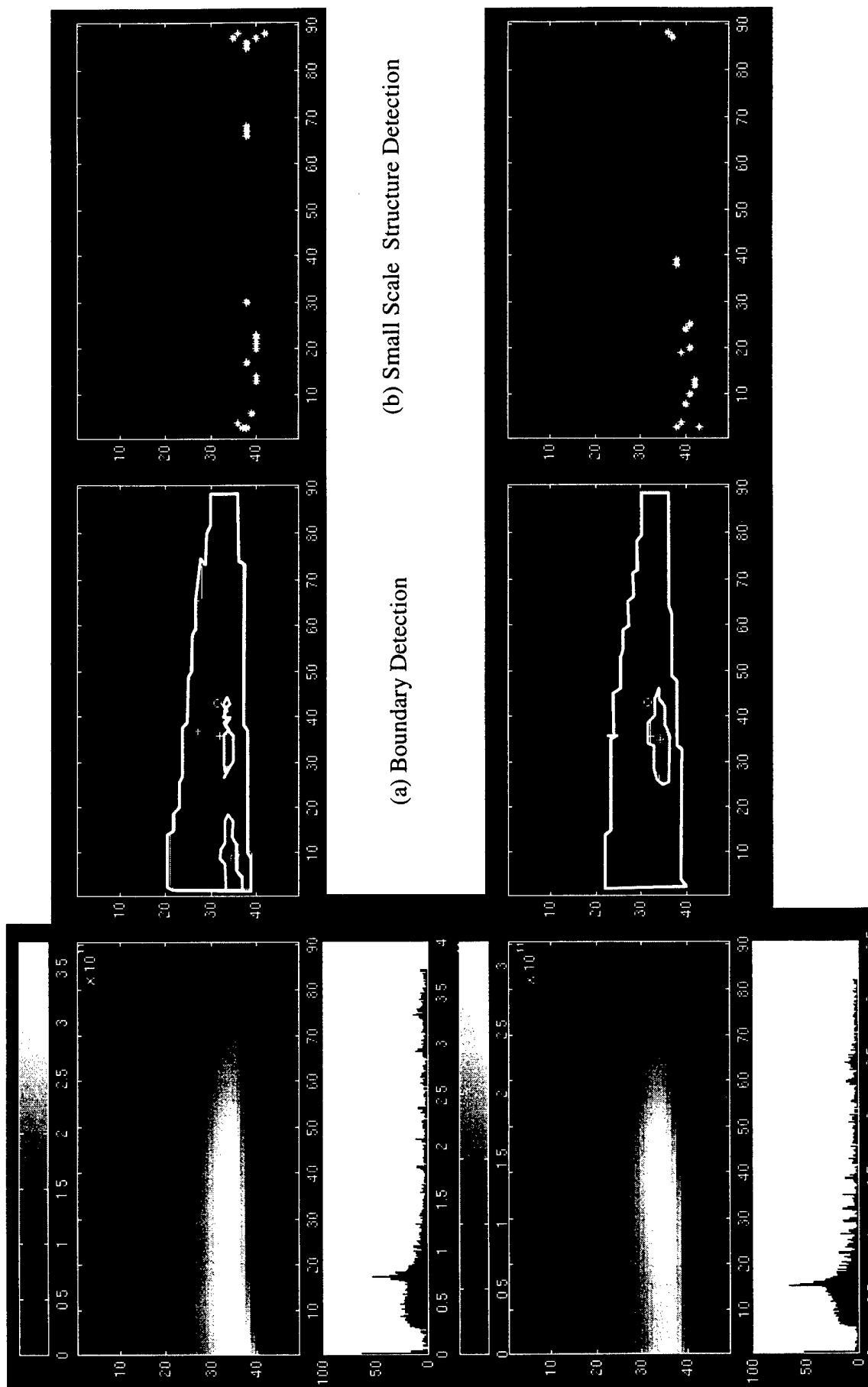


Figure 7. Boundary Detection of Peaks and Band. (b) Detection of Small Scale Disturbances.

02 07 15:48

FEATURE EXTRACTION RESULTS

Quality	Parameter	Images
7.8	ri226.0.vol.raw: 2	
3.9	ri226.2.vol.raw: 2	
0.39595		

Images
ima02.0_2-ima05.4_2.comp
ri226.0_2-ri226.2_2.comp

BANDS

	GeoCtr-X	GeoCtr-Y	ValCtr-X	ValCtr-Y	MajAx-L	MajAx-O
IMAGE 1						
BAND 1	31.41	43.09	31.89	35.64	88.12	-9.14
IMAGE 2						
BAND 1	31.58	42.87	32.00	35.45	88.12	-9.14

PEAKS

	GeoCtr-X	GeoCtr-Y	ValCtr-X	ValCtr-Y	MajAx-L	MajAx-O
IMAGE 1						
PEAK 1	35.37	9.57	34.45	8.90	16.28	-169.38
PEAK 2	0.00	0.00	0.00	0.00	0.00	0.00
IMAGE 2						
PEAK 1	35.00	35.85	34.15	34.72	20.02	-177.14

TIDS

IMAGE 1: 21 IMAGE 2: 15

Figure 8. Results of Feature Extraction.

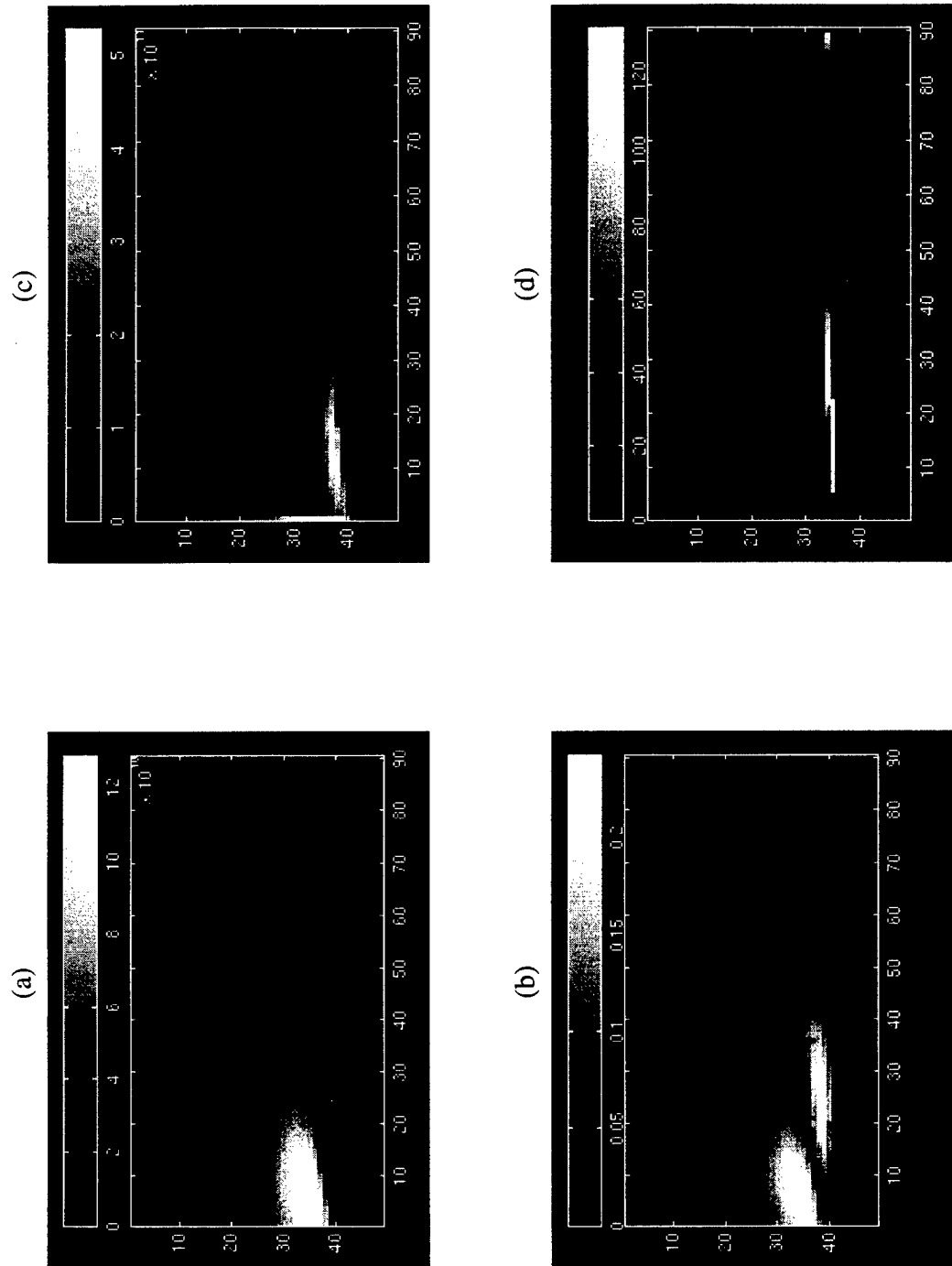


Figure 9. Difference Images of Ionospheric Distributions Shown in Figure 3. (a) Absolute Square Difference Image (b) Normalized Square Difference Image (c) Magnitude of Gradient Error Image (d) Orientation of Gradient Error Image.

Feature	Image	Attributes	Significance
Band	original	boundary, centroid, valtroid, maj. ax. length & slope	band existence
Peak	original	boundary, centroid, valtroid, maj. ax. length & slope	peak existence
Patch	original	position, electron density	patch existence
ASE Pocket	ase	boundary, centroid, valtroid, maj. ax. length & slope	value recovery
NSE Pocket	nse	boundary, centroid, valtroid, maj. ax. length & slope	shape recovery
MAG Pocket	absgrme	boundary, centroid, valtroid, maj. ax. length & slope	grd. mag. recovery
SLP Pocket	absgrae	boundary, centroid, valtroid, maj. ax. length & slope	grd. orient. recovery
Maxdensity	original	3D (4D) plot of Ne vs latitude, altitude (&longitude)	F_2 critical frequency

Table 1. Features Selected for Representing Contents of Ionospheric Images.